

in less deformation. Cells with surfaces nearly parallel to the average flow direction interact with the post over a greater area and longer time, resulting in more significant deformation.

We now turn to examine the effect of post shape on erythrocyte displacement into the product at high flow velocities in the next section. In Section 4.6, we discuss which post shapes give the best combination of high leukocyte yield and low erythrocyte contamination in the product output.

























4.5 Dependence of the Erythrocyte Contamination of the Product Output on Post Shape at High Flow Rates

In this section, we experimentally determine and fundamentally explain how post geometry contributes to erythrocyte contamination of the product at high flow rates.

4.5.1 Experimental Dependence on Post Shape at High Flow Rate

We use DLD arrays with parameters described in Table 4.2 to examine the effect of post geometry on erythrocyte contamination of the product at Re greater than 1. These array parameters were originally used for harvesting PC3 cancer cells from blood, which have a much larger critical size of $\sim 17 \mu\text{m}$ [52] than one would have for harvesting leukocytes ($\sim 4.5 \mu\text{m}$). Nevertheless, the lessons we learn here about undesired contamination of erythrocytes into the product output applies to designs with smaller critical sizes, as will be shown in Section 4.6. In the PC3 cancer cell harvesting project, which is described in Section 3.5 of Chapter 3, we originally used asymmetric triangular posts because they allow for a wider gap for a fixed critical

Table 4.4: Erythrocyte contamination of the product and displacement of polymer microspheres (beads) below the critical size of the DLD array into the product for different post geometries under the same experimental conditions. Array parameters are $62\ \mu\text{m}$ posts, $36\ \mu\text{m}$ gaps, and $1/26$ tilt for all post geometries. The average flow velocity in the gap is $42.9\ \text{cm/s}$, the Reynolds number is 15.4, and the average shear rate is $24000\ \text{s}^{-1}$ for all post geometries.

Tilt	Post	Flow	Geometry	% RBCs in Product	% $5.7\ \mu\text{m}$ Beads in Product
			Asymmetric Triangle	4.9	4.6
			Circle	0.03	0.01
			Rounded Triangle	52.3	33.7
			Extended Semi-Circle	0.04	0.03
			Upright Triangle	3.1	--
			Quarter Circle	0.03	--
			Downturned Triangle	65.2	39.6
			Square	0.43	--

size and tilt angle, leading to higher flow rates for a fixed applied pressure and less clogging due to cell adhesion to the posts. However, we noticed surprisingly high erythrocyte contamination of the product that did not decrease even as we increased the critical size of the asymmetric triangular post array from $6\ \mu\text{m}$ to $7.5\ \mu\text{m}$ by changing the array tilt while keeping the flow Re constant, implying that the cause of the erythrocyte displacement was hydrodynamic as opposed to bumping. When we changed the asymmetric triangular posts to conventional circular posts of the same size, the erythrocyte contamination of the product diminished by a factor of 150 for the same flow Re . This motivated us to investigate the effect of post shape on erythrocyte displacement in DLD arrays as Re increases above 1.

The length of the array is $38.2\ \text{mm}$, and the width is $2.3\ \text{mm}$. The experimental conditions at which erythrocyte contamination of the product is measured are that

the average flow velocity in the gap is 42.9 cm/s, the Reynolds number (gap width * average flow velocity in the gap / kinematic viscosity of water) is 15.4, and the average shear rate (average flow velocity in the gap / half the width of the gap) is 24000 s⁻¹. The results for the eight post geometries tested are shown in Table 4.4.

Reorientation of erythrocytes by post shapes can change their apparent size and behavior in the DLD array [88, 70]. The shapes and motion of erythrocytes in microfluidic devices at various flow rates, including the effects of inertial lift forces at moderate Reynolds numbers, has been studied extensively [22]. Recently, the behavior of erythrocytes in DLD arrays has been examined through simulation studies at low Reynolds numbers [42, 92]. In order to determine the extent to which qualitative types of erythrocyte behavior contribute to the effects we observe here, we run the same experiments with 5.7+/-0.38 μm non-deformable polymer microsphere beads, which are well below the critical size of the array for all post shapes considered. The displacement of the polymer microsphere beads into the product very closely tracks the displacement of erythrocytes into the product (Table 4.4), which shows that effect of post shape on erythrocyte displacement is not due to reorientation of erythrocytes by the posts or other specific flow-velocity-dependent behavior, such as shape changes, of erythrocytes.

The main observation from these experimental results (Table 4.4) is that the fraction of erythrocytes displaced into the product (vs. the erythrocytes input into the DLD array) varies by a factor of over 2000, from 0.03% to 65.2%. In analyzing these results, we consider symmetry about an axis parallel to the average flow direction, and the terms “symmetric” and “asymmetric” are used to refer to the existence or non-existence, respectively, of symmetry about this axis (Symmetry about an axis perpendicular to the flow direction is referred to as “up-down symmetric”). Note that erythrocyte contamination of the product is significantly higher for asymmetric triangular post geometries than for symmetric and asymmetric but very rounded post

geometries. Even though square posts have sharp corners, the erythrocyte displacement into the product with square posts is at least an order of magnitude less than with any of the asymmetric triangular post geometries, indicating that hydrodynamic asymmetry is a significant driver of erythrocyte contamination of the product. By hydrodynamic asymmetry, we mean that the post shape is asymmetric such that the curvature of the streamlines entering the gap around the bumping side of the post at one side of the gap is very different than the curvature of the streamlines entering the gap around the non-bumping side of the post at the opposite side of the gap.

4.5.2 Experimental Dependence on Flow Rate and Post Symmetry

We now examine the dependence of the undesired erythrocyte collection in the product output on flow velocity. For reference, Re of 1 corresponds to an average flow velocity in the gap of 2.9 cm/s, and Re of 20 corresponds to an average flow velocity in the gap of 58.8 cm/s.

The fraction of erythrocytes displaced into the product is shown as a function of Re for DLD arrays with asymmetric triangular and circular posts with the same post size, gap size, and tilt angle (Figure 4.12). First, we note that for conventional circular posts there is little erythrocyte contamination of the product at all Re. For asymmetric triangular posts, even at Re of 1, there is measureable (concentration $> 1 \times 10^4 \text{ mL}^{-1}$) erythrocyte contamination of the product. With asymmetric triangular posts, the erythrocyte contamination increases significantly with Re before leveling off at $\text{Re} \sim 10$, with approximately 5% of erythrocytes in the product. With circular posts, the fraction of erythrocytes in the product increases very slowly with Re, never exceeding 0.03% of erythrocytes (concentration: $1.1 \times 10^5 \text{ mL}^{-1}$) even at Re of 20, which is an order of magnitude less than the fraction of erythrocytes appearing in

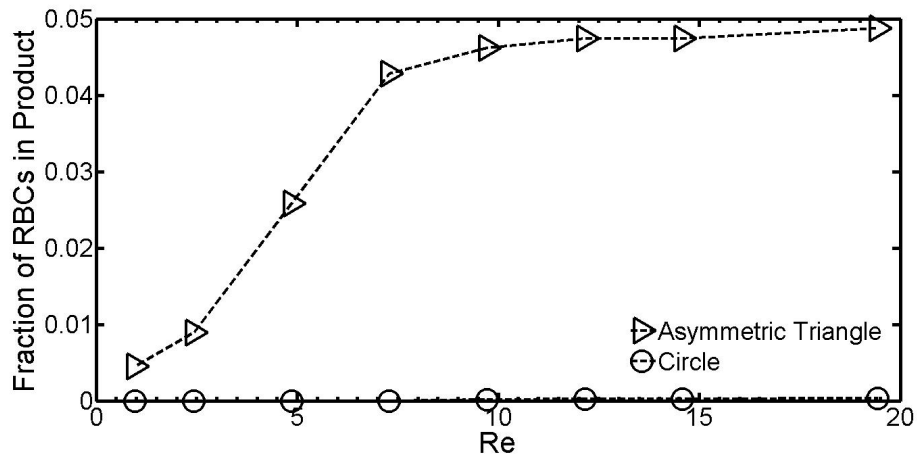


Figure 4.12: Fraction of erythrocytes in the product vs. Re for asymmetric triangular posts and circular posts. The fraction of erythrocytes in the product increases significantly with Re for asymmetric triangular posts but not for circular posts. The asymmetric triangular posts are isosceles triangles with height (in the direction of the flow) and width (perpendicular to the direction of the flow) of $62 \mu\text{m}$, and the gap is $36 \mu\text{m}$. The circular post array has $62 \mu\text{m}$ diameter circular posts with $36 \mu\text{m}$ gaps. The tilt is $1/26$ for both asymmetric triangular and circular post arrays.

the product with asymmetric triangular posts at Re of 1 and is mainly comprised of small clumps of 3-5 erythrocytes.

This confirms that the high undesirable lateral displacement of erythrocytes into the product with asymmetric triangular posts is a high flow velocity ($1 < Re < 20$) effect. From this section and the previous section, we have learned that erythrocyte displacement into the product occurs in a flow-velocity-dependent manner for post shapes that lack symmetry about an axis parallel to the average flow direction. Further, this effect is not due to the reorientation of erythrocytes by certain post shapes or the specific velocity-dependent behavior of erythrocytes, as similar behavior is observed for non-deformable polymer microspheres.

4.5.3 Modelling

Model Definition

In Section 4.2.4, we showed that a particle following a streamline is acted upon by a viscous drag force, which keeps the particle near the streamline, and a centripetal acceleration force, which causes the particle to travel perpendicular to the streamline with lateral velocity, v_L . For an erythrocyte, this lateral velocity, v_L is given by:

$$v_L = \frac{(\rho_{RBC} - \rho_f)V_{RBC}a_c}{6\pi\mu R_{RBC}} \quad (4.15)$$

where ρ_{RBC} and ρ_f are the densities of the erythrocyte ($1.13 \times 10^3 \text{ kg/m}^3$) and fluid ($1.03 \times 10^3 \text{ kg/m}^3$), respectively, V_{RBC} is the volume of the erythrocyte ($1.10 \times 10^{-16} \text{ m}^3$), a_c is the centripetal acceleration, μ is the dynamic viscosity of the fluid ($1 \times 10^{-3} \text{ kg/(m}\cdot\text{s)}$), and R_{RBC} is the radius of the erythrocyte ($5 \times 10^{-6} \text{ }\mu\text{m}$).

Using the 2-D velocity surface in COMSOL (without any particles), which is described in Section 4.3.3, as the input, we numerically evaluate a_c by tracing fluid paths starting across the width of one gap into the subsequent gap in the direction of the flow (Figure 4.13). The 2-D velocity surface encodes the x and y components of the velocity at $1 \text{ }\mu\text{m}$ intervals in both the x and y directions. The fluid path is traced by multiplying the x and y components of the velocity at the current point by the time to travel $1 \text{ }\mu\text{m}$ in the y-direction (which is the flow direction), which is equal to $1 \text{ }\mu\text{m}$ divided by the y-component of the velocity at the current point. Although the grid spacing is $1 \text{ }\mu$, weighted averages of the two nearest points on either side of the current point along the x-axis are used in tracing the fluid to the next point in the y-direction. The total acceleration vector is then computed by the vector difference between the velocity at the next point and the velocity at the current point divided by the time to travel between the two points, which is $(1 \text{ }\mu\text{m})/v_y$, where v_y is the average of the y-velocities at the current and next points. The centripetal acceleration

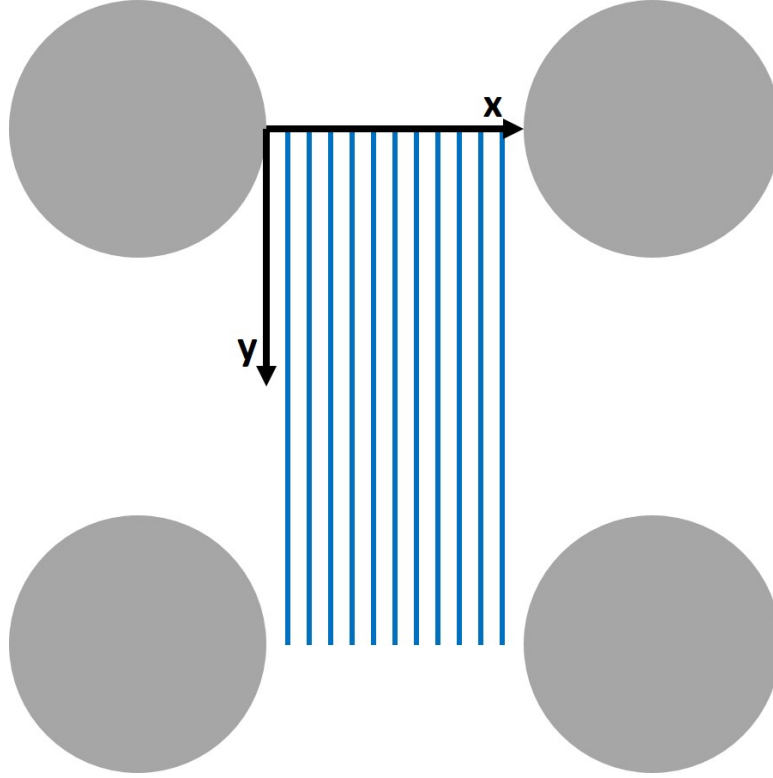


Figure 4.13: A DLD array with zero tilt is shown to illustrate tracing of fluid paths from one gap to the next in the direction of the flow to enable calculation of the centripetal acceleration. Flow is along the y -axis. Fluid paths, shown in blue, are traced at equally spaced points along the x -axis from one gap to the subsequent gap in the direction of the flow. The fluid paths are shown as straight lines for illustrative purposes. The actual fluid paths are traced numerically using data from the 2-D velocity surfaces computed in COMSOL, which is described in Section 4.3.3.

can then be computed from the dot product between the total acceleration and the vector average of \mathbf{n}_1 , which is the unit normal to the velocity vector at the current point, and \mathbf{n}_2 , which is the unit normal to the velocity vector at the next point.

We have now calculated the centripetal acceleration, a_c , at $1 \mu\text{m}$ intervals along each of the paths that we seek to evaluate. From equation 4.15, we can calculate the lateral velocity of the erythrocyte induced by the centripetal acceleration at each point. We now seek the total lateral displacement of the erythrocyte over each fluid path we trace from one gap to the subsequent gap in the direction of the flow. In order to calculate this, we have to evaluate the integral (See Section 4.2.4):

$$x_L = \int v_L d\left(\frac{y}{v_y}\right) \quad (4.16)$$

over each path from one gap to the subsequent gap in the direction of the flow. Here, distance in the direction of the flow (vertical) and v_y is the velocity in the direction of the flow (vertical).

Note that our model defines positive centripetal acceleration ($a_c > 0$) for fluid with increasing velocity curving to the left as the fluid moves through the gap and negative centripetal acceleration ($a_c < 0$) for fluid with increasing velocity curving to the right as the fluid moves through the gap.

Model Application

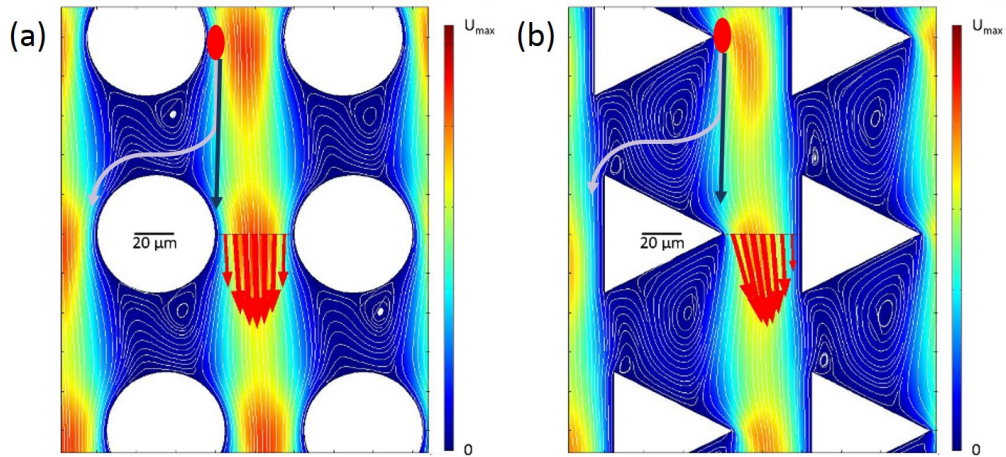


Figure 4.14: Surface plots of the magnitude of the fluid velocity in a DLD array with $60 \mu\text{m}$ posts, $40 \mu\text{m}$ gaps, and $1/20$ tilt at Re of 20 for (a) circular posts and (b) asymmetric isosceles triangular posts. The erythrocyte shown in red should take the zig-zag path, which is shown in silver, leading it to the waste output. At this Re , it often instead takes the black path with asymmetric triangular posts but not with circular posts, leading it to the product output. Note that the velocity vectors across the narrowest width of the gap shown in red are oriented nearly entirely vertically for circular posts but have a significant horizontal component for asymmetric triangular posts.

Asymmetric triangular posts are often used in DLD array because compared with circular posts, asymmetric triangular posts offer a larger gap for a given critical size and tilt angle [49]. Because both asymmetric triangular posts and circular posts are popular and because there is a very large ($>100X$) difference in undesired erythrocyte displacement into the product at Re of 15 between arrays with these two post shapes, we first focus our attention on these two post shapes.

Surface plots of the fluid velocity in DLD arrays with circular and asymmetric triangular posts at Re of 20 are shown in Figure 4.14. At Re of 20, the fluid bends around the two post shapes into the gap in different ways, as shown by the red arrows. With circular posts, the red arrows are relatively vertical across the width of the gap. However, with asymmetric triangular posts, the red arrows closest to the vertex of the triangle (the bumping side of the post) indicate that the velocity here has a significant horizontal component. Below the gap, the vectors point back to the left. We seek to evaluate if the centripetal acceleration from the fluid bending around the asymmetric triangular post in this way contributes to the higher displacement of erythrocytes into the product.

In order to make this evaluation, we evaluate, for both circular and asymmetric triangular post arrays, the integral in Equation 4.16 over each of 39 fluid paths that we trace from one gap to the next in the flow direction starting at $1 \mu\text{m}$ intervals across the width of the first gap using the 2-D surface plot of the fluid velocity in Figure Figure 4.14 ($Re = 20$). This method is schematically illustrated in Figure 4.13. The values of x_L for each of the 39 paths that we trace starting at $1 \mu\text{m}$ intervals across the width of the first gap for circular and asymmetric triangular posts are shown below in Figure 4.15.

For displacement of a particle from the “slingshot” effect to be large enough for the particle to reach the product output, in each unit cell it would have to be displaced as much as if it were a large particle bumping normally. x_L over one period would have

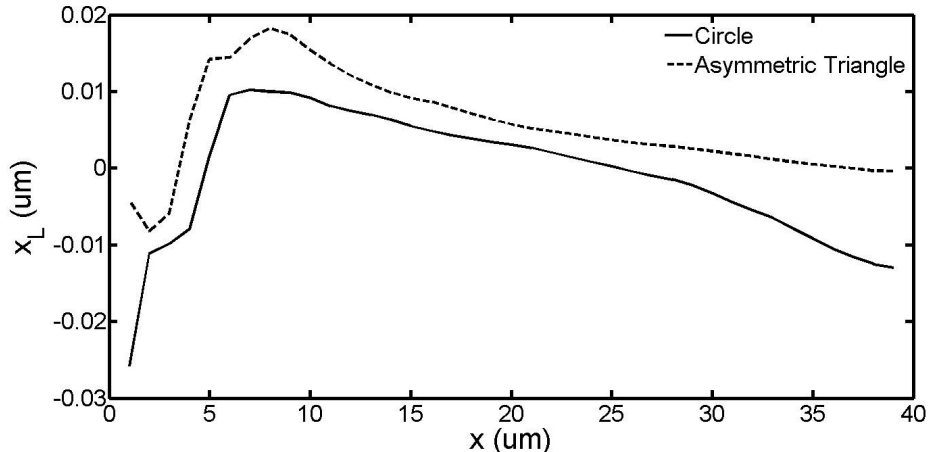


Figure 4.15: Total lateral displacement, x_L , of the erythrocyte due to centripetal acceleration as fluid is traced from a point x μm into the gap from the bumping side of a post to the subsequent gap in the direction of the flow. The flow velocity corresponds to Re of 20. Negative x_L for small values of x results from tracing fluid that zig-zags to the next gap opposite the tilt direction instead of flowing into the next gap following the tilt.

to equal, on average, the tilt angle times the gap size, which is $1/20 \times 40 \mu\text{m} = 2 \mu\text{m}$ in this case. For both asymmetric triangular posts and circular posts at Re of 20, x_L does not exceed $0.02 \mu\text{m}$ for any of the 39 paths that we trace from one gap into the next in the direction of the flow (Figure 4.15). This is two orders of magnitude too small for displacement of erythrocytes into the product to result from the “slingshot” effect. Thus, we conclude that this conceptually simple mechanism is not responsible for the undesired erythrocyte contamination, assuming our assumption that the particle does not disturb the flow distribution is correct.

4.5.4 Other Post-Shape-Dependent High Flow Rate Effects

Although the flow rate is too small by two orders of magnitude for inertial (shear-gradient and wall effect) lift forces to affect particle trajectories for the array parameters considered here, hydrodynamic effects due to asymmetry, such as those involved in non-inertial lift cell sorting [19, 21] and pinched flow fractionation [86, 80, 66],

are still possible. Since the tilt angle is shallow (tilt angle $< 1/20$) in our work, for circular posts, fluid enters the gap at one side of the gap with centripetal acceleration of similar magnitude but opposite sign as at the opposite side of the gap. However, for asymmetric triangular posts, the fluid has a significantly higher centripetal acceleration around the vertex pointing into the gap from the bumping side of the post compared to fluid entering around the flat side of the asymmetric triangular post at the opposite side of the gap. This is similar to the conditions for pinched flow fractionation described in Section 4.2.3.

Note that “centripetal acceleration” is in some sense a proxy for “curvature” of the streamlines and hydrodynamic effects in general, as would cause pinched flow effects. Therefore, we examine how centripetal acceleration varies in the array with different post geometries. For simplicity, we examine the centripetal acceleration of the fluid across the narrowest point of the gap, not the entire unit cell as in the previous section.

We first examine the flow velocity dependence of erythrocyte contamination of the product with circular and asymmetric triangular posts and how this relates to the centripetal acceleration distribution in the gap between the posts for each of these two post shapes. We then alter the degree of asymmetry of fluid entering the gap by altering the up-down symmetry (symmetry about an axis perpendicular to the flow direction) of the asymmetric triangular posts and by altering the roundedness of the triangular posts. Finally, we show that it is the combination of sharp corners and post asymmetry that causes significant erythrocyte contamination of the product at high flow velocities corresponding to $Re > 1$.

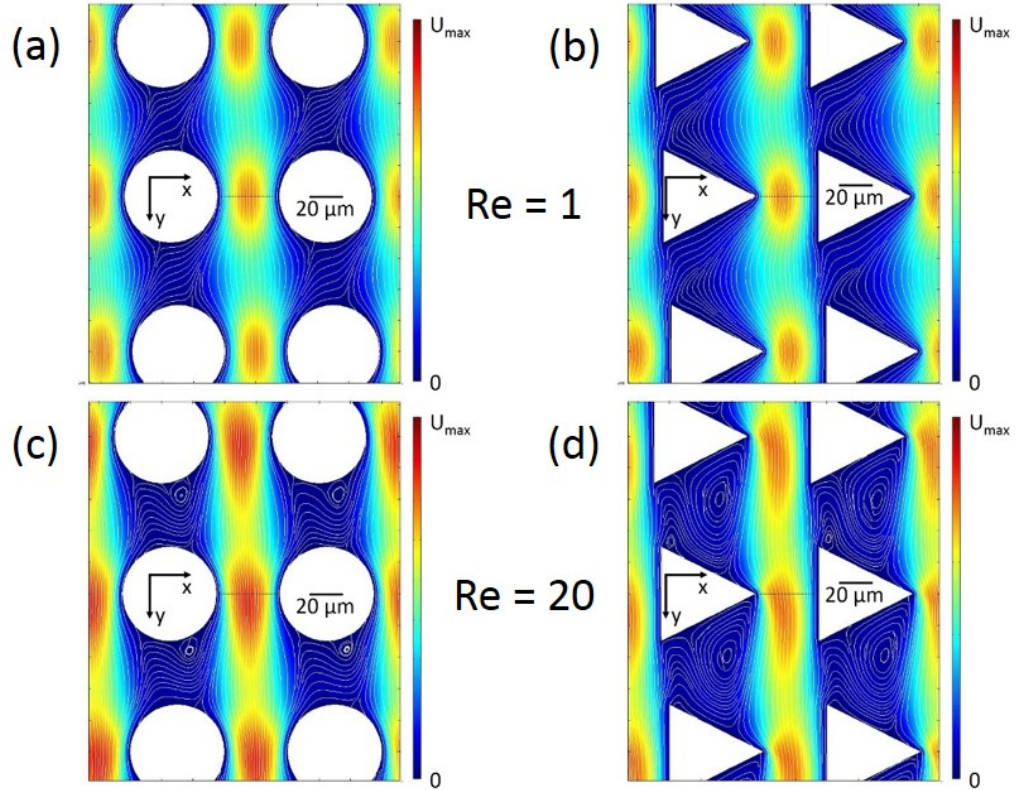


Figure 4.16: Surface plots of fluid velocity in a DLD array with $60 \mu\text{m}$ posts, $40 \mu\text{m}$, and $1/20$ tilt for (a) circular posts at Re of 1, (b) asymmetric triangular posts at Re of 1, (c) circular posts at Re of 20, and (d) asymmetric triangular posts at Re of 20.

Flow Velocity Dependence of Erythrocyte Contamination of the Product with Circular and Asymmetric Triangular Posts

We showed in Section 4.5.2 that erythrocyte contamination of the product increases significantly with Re in DLD arrays with asymmetric triangular posts but not in DLD arrays with circular posts. In order to better understand this effect, we begin by examining surface plots of the fluid velocity in DLD arrays with asymmetric triangular and circular posts at Re of 1 and 20 (Figure 4.16). For circular posts, the main difference between the surface plots of the fluid velocity at Re of 1 (Figure 4.16(a)) and Re of 20 (Figure 4.16(c)) is that at Re of 20, the high velocity region in the gap between the posts is elongated compared to the high velocity region in the gap

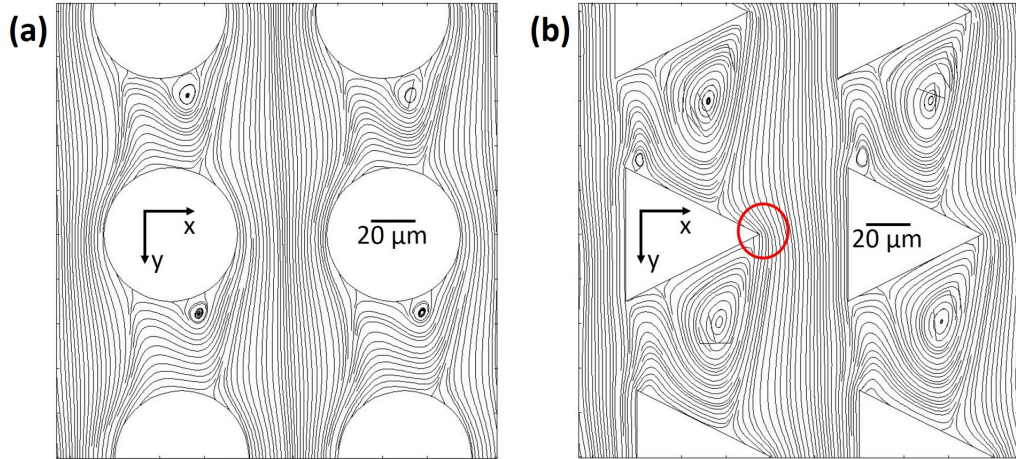


Figure 4.17: Streamline plots in a DLD array with $60 \mu\text{m}$ posts, $40 \mu\text{m}$, and $1/20$ tilt for (a) circular posts and (b) asymmetric triangular posts at Re of 20. Note that with circular posts, the curvature of the streamlines in the gap is relatively small, and the magnitude of the curvature of the streamlines at opposite sides of the gap is similar. In contrast, the streamlines coming around the vertex of the asymmetric triangular post at the left side of the gap have substantial curvature (circled in red), while the streamlines coming around the flat side of the asymmetric triangular post at the right side of the gap have almost no curvature.

between the posts at Re of 1. This occurs because the inertia of the fluid prevents it from spreading out in the subsequent region following the gap in the direction of the flow (vertical). With asymmetric triangular posts, we can see from the surface plots of the fluid velocity at Re of 1 (Figure 4.16(b)) and at Re of 20 (Figure 4.16(d)) that this inertia of the fluid has an additional effect, which causes the high velocity region in the gap between the posts at Re of 20 to be asymmetric. At Re of 20, the fluid coming around the vertex of the post on the left side of the gap has substantial curvature compared to fluid entering the gap around the flat side of the post at the right side of the gap (Figure 4.17). This leads us to examine how the centripetal acceleration distribution changes with Re for circular and asymmetric triangular post shapes (Figure 4.18).

With the symmetric circular posts, the centripetal acceleration distribution in the gap is similar at Re of 1 and Re of 20, with the only significant difference being in the

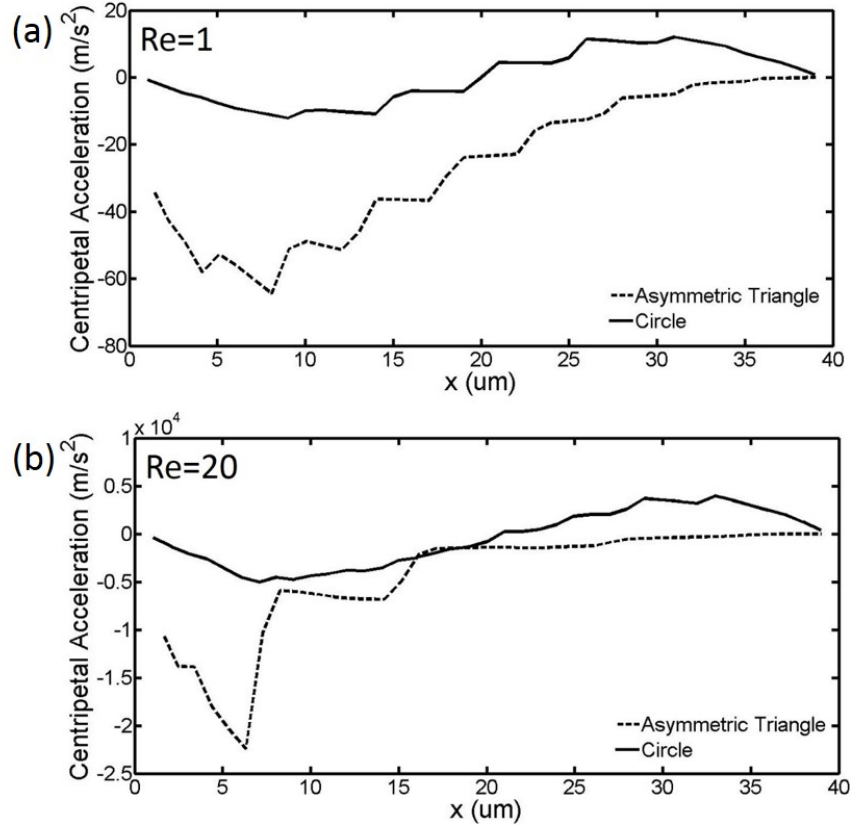


Figure 4.18: The acceleration of the fluid perpendicular to the streamlines (centripetal acceleration) in the gap between the posts is plotted as a function of distance from the bumping side of the post for circular posts and asymmetric triangular posts for (c) $\text{Re}=1$ and (d) $\text{Re}=20$. For the asymmetric triangular posts, note that the centripetal acceleration distribution is broadly spread across the gap at Re of 1, but is mostly confined to a region extending $7 \mu\text{m}$ into the gap from the bumping side of the post at Re of 20. In contrast, the centripetal acceleration distribution in the gap for circular posts is similar at Re of 1 and Re of 20, with the main difference being the magnitude of the centripetal acceleration.

magnitude of the centripetal acceleration. The centripetal acceleration of the fluid around the bumping side of the post at one side of the gap is approximately equal in magnitude to the centripetal acceleration of the fluid around the non-bumping side of the post at the opposite side of the gap at both Re of 1 and Re of 20. With the asymmetric triangular posts, the centripetal acceleration distribution is spread broadly across the gap at Re of 1, but is mostly confined to a region extending $7 \mu\text{m}$ into the gap from the bumping side of the post at Re of 20, which represents

about 1/20 of the total flow through the gap by volume. This results from the centripetal acceleration around the vertex that comprises the bumping side of the post for the asymmetric triangular post increasing rapidly with Re while the centripetal acceleration around the flat side of the asymmetric triangular post at the opposite side of the gap remains at approximately zero. Because the shape of the centripetal acceleration distribution across the gap qualitatively matches the observed effect of erythrocyte contamination of the product vs. flow rate (Section 4.5.2) for circular vs. asymmetric triangular posts, we strongly suspect that it is related to the underlying mechanism. In the next two sections, we examine, using other post shapes, how geometry-induced changes in the centripetal acceleration around the bumping side of the post at a fixed Re affect erythrocyte contamination of the product.

Effect of Up-Down Asymmetry of Left-Right Asymmetric Triangular Posts on Erythrocyte Contamination of the Product

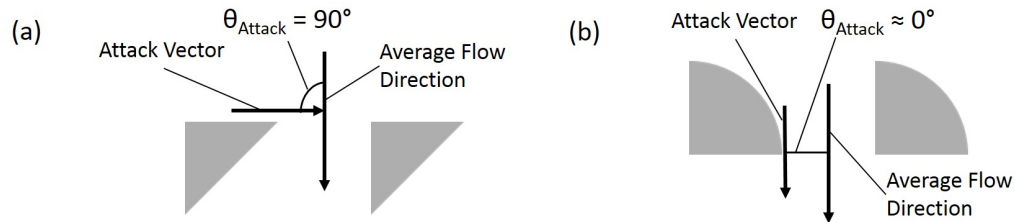


Figure 4.19: Definition of fluid “angle of attack” illustrated in a DLD array with (a) downturned triangular posts, which have a θ_{Attack} of 90° , and (b) quarter circular posts, which have a θ_{Attack} of $\sim 0^\circ$.

In this section, we examine the effect of up-down symmetry (symmetry about an axis perpendicular to the flow) of left-right asymmetric triangular posts on erythrocyte contamination of the product. We begin with the up-down symmetric left-right asymmetric triangular post (Figure 4.20(a)) that we have used so far in this chapter, and break the up-down symmetry in two ways to create downturned triangular posts(Figure 4.20(b)) and upright triangular posts(Figure 4.20(c)). In order to exam-

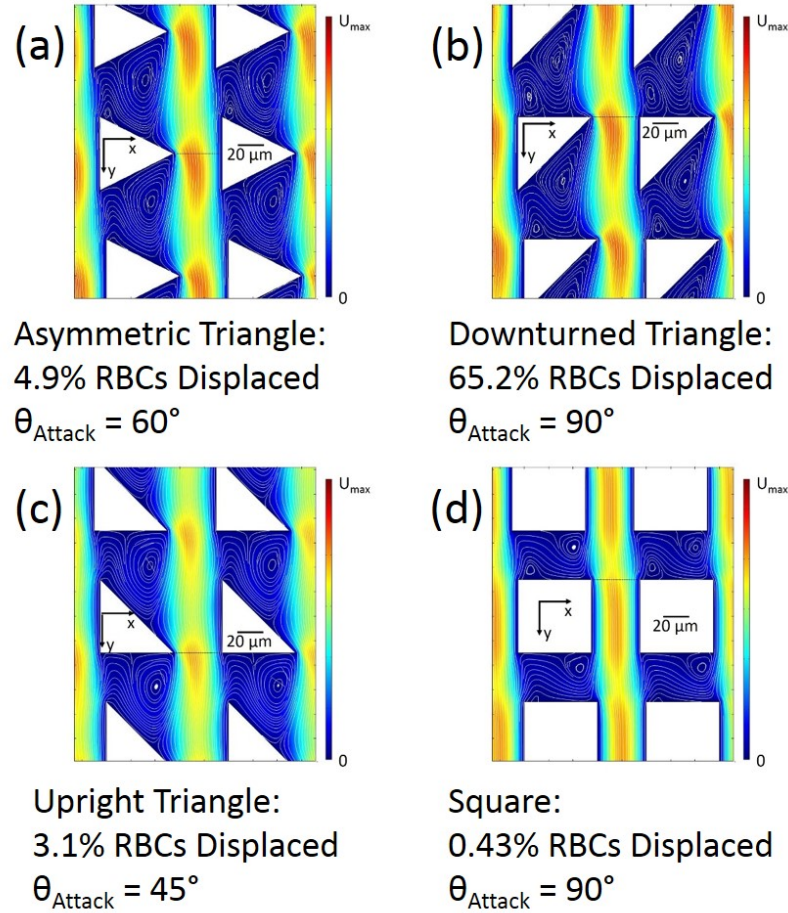


Figure 4.20: Surface plots of fluid velocity in a DLD array with $60 \mu\text{m}$ posts, $40 \mu\text{m}$ gaps, and $1/20$ tilt at Re of 20, the experimentally observed fraction of erythrocytes displaced into the product at Re of 15, and the fluid “angle of attack” for (a) asymmetric triangular posts, (b) downturned triangular posts, (c) upright triangular posts, and (d) square posts.

ine the effect of sharp corners on erythrocyte contamination of the product, we then compare erythrocyte contamination of the product with these three post shapes to erythrocyte contamination of the product with a square post (Figure 4.20(d)) instead of a circular post.

Analysis of the surface plots of fluid velocity in DLD arrays with these four posts shapes yields qualitative insights into the physical mechanism driving erythrocyte contamination of the product. We begin by looking at the angle between the average flow direction (vertical) and the tangent to the upstream face of each of these four

post shapes, which we call the “angle of attack” 4.19, and how this angle relates to undesired erythrocyte displacement. With downturned triangles, this angle is 90° , the largest for these four post shapes, and the undesired erythrocyte displacement is similarly the largest at 65.2%. For the up-down symmetric left-right asymmetric triangle and the upright triangle, these angles are 60° and 45° , respectively, and the undesired erythrocyte displacements are 4.9% and 3.1%, showing a clear, monotonic relationship between the angle of attack and undesired erythrocyte displacement. For square posts, however, the angle of attack is 90° , and the undesired erythrocyte displacement is only 0.43%. Thus, we conclude that, qualitatively, there is a strong, direct relationship between the angle of attack and undesired erythrocyte displacement for left-right asymmetric (asymmetric about an axis parallel to the flow direction) post shapes. Comparing erythrocyte displacement with square posts to erythrocyte displacement with circular posts, we conclude that this relationship between angle of attack and erythrocyte displacement is much weaker for left-right symmetric post shapes, and as we saw in the previous section with circular posts, post shapes with left-right symmetry have low erythrocyte contamination of the product output.

From these results, it is clear that left-right post shape asymmetry is driving undesired erythrocyte displacement, and we now examine the centripetal acceleration distribution in the gap to understand how hydrodynamic effects resulting from “curvature” of the streamlines may be contributing to this effect (Figure 4.21).

For the three left-right asymmetric triangular post shapes we consider, the angle of attack is a proxy for the amount of fluid that experiences high centripetal acceleration in entering the gap around the vertex that comprises the bumping side of the post. Since the vertical velocity profile across the width of the gap is parabolic, most of the fluid flows through the middle of the gap, with very little flowing at the sides of the gap. Thus, one way to determine how much fluid experiences high centripetal acceleration entering the gap around the bumping side of the post is to look at how

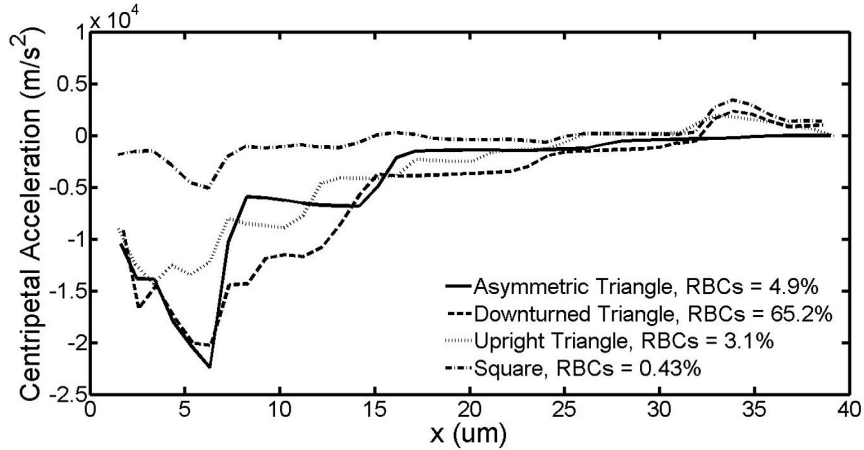


Figure 4.21: The acceleration of the fluid perpendicular to the streamlines (centripetal acceleration) in the gap is plotted as a function of distance from the bumping side of the post for asymmetric triangular, downturned triangular, upright triangular, and square post geometries at $Re=20$. Note that for the square post, the centripetal acceleration is computed across the top of the gap, where the black line is shown in Figure 4.20(d).

far into the gap from the bumping side of the post the high fluid centripetal acceleration extends. From Figure 4.21, we see that, qualitatively, the high fluid centripetal acceleration region extends much farther into the gap for the downturned triangle than for the up-down symmetric asymmetric triangle and the upright triangle, which have centripetal acceleration distributions in the gap that are much more similar. In section 4.5.5, we quantify this measure of the volume of fluid experiencing high centripetal acceleration by integrating the centripetal acceleration multiplied by the vertical velocity (how much fluid flows in that region) over the width of the gap and show that this value correlates well with undesired erythrocyte displacement.

The relationship between the fluid centripetal acceleration distribution in the gap and undesired erythrocyte displacement can also be viewed in terms of symmetry of the fluid centripetal acceleration distribution in the gap. In each of the three left-right asymmetric triangular post shapes we examine in this section, the centripetal acceleration at the right side of the gap is limited to small values due to the “no-

slip” condition at the flat side of the asymmetric triangle bounding that side of the gap. Therefore, how far into the gap from the bumping side of the post the high fluid centripetal acceleration region extends is also a measure of the asymmetry of the fluid centripetal acceleration distribution with respect to an axis parallel to the flow direction and passing through the center of the gap ($x = 20 \mu\text{m}$ in Figure 4.21). In contrast to the three left-right asymmetric triangular post shapes, the square post has a nearly symmetric fluid centripetal acceleration distribution in the gap by this definition.

The relatively low (0.43%) undesired erythrocyte displacement for square posts is interesting for three reasons. First, it shows that the relationship between angle of attack and undesired erythrocyte displacement is much weaker for left-right symmetric post shapes than for left-right asymmetric post shapes. Second, it had been suggested that sharp corners on post shapes can induce flipping of erythrocytes, resulting in undesired displacement [70, 88]. This result shows that this is not a major contributor to undesired erythrocyte displacement. Third, the relatively low erythrocyte displacement into the product with square posts provides further evidence that lift effects arising from interactions with the walls of the posts do not play a significant role in erythrocyte displacement into the product at high flow rates [92, 7]. Compared to other post shapes, square posts provide the most wall area (wall area along the entire length of the gap) that can exert a force on erythrocytes perpendicular to the flow direction, causing the erythrocytes to cross streamlines, yet this results in displacement of only 0.43% of erythrocytes.

Effect of Roundedness of Asymmetric Triangular Posts on Erythrocyte Contamination of the Product

The “roundedness” of the asymmetric triangular posts is important because it is often determined by the process used to fabricate DLD arrays and has been shown to

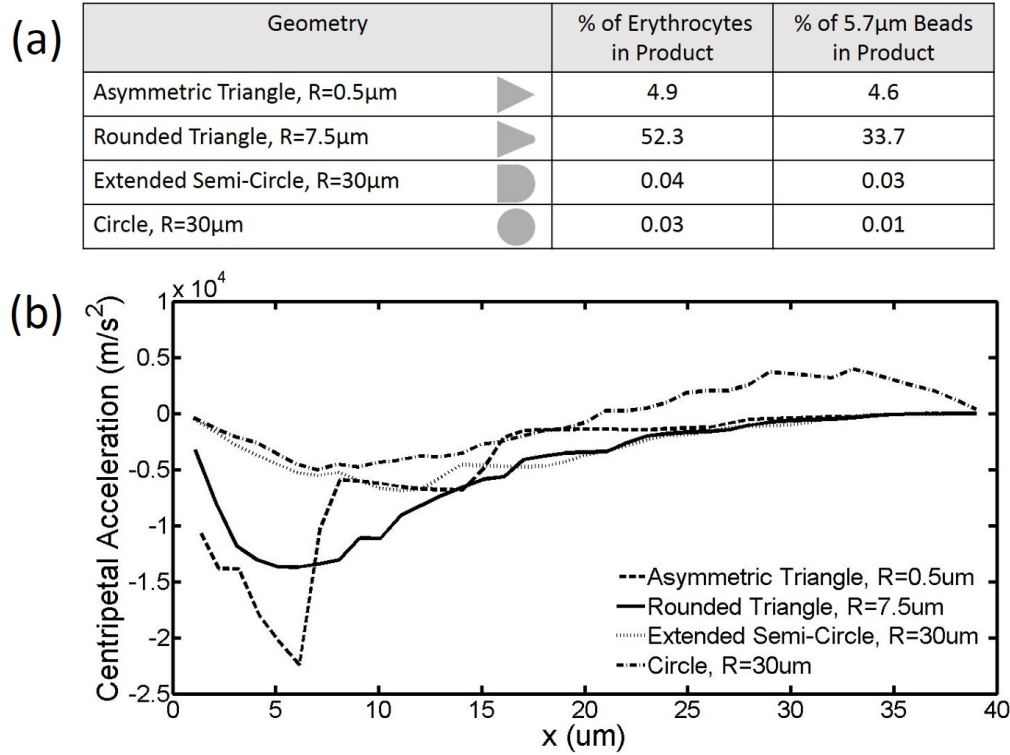


Figure 4.22: (a) As the roundedness of the asymmetric triangle increases from 0.5 μm , which is the experimental fabrication limit, to 30 μm , which renders the asymmetric triangle effectively a combination of half of a square and half of a circle (“extended semi-circle”), the erythrocyte contamination increases by a factor of 10 before decreasing to an amount comparable to that with circular posts. This effect is not unique to erythrocytes and also occurs for spherical beads with a diameters of 5.7 \pm 0.38 μm , which is well below the critical size of the array for all post geometries examined here. (b) Centripetal acceleration of the fluid versus distance into the gap from the bumping side of the post for each of the four post geometries in (a) at Re of 20.

affect the critical size of the array [49]. The effect of the roundedness of asymmetric triangular posts on the behavior of erythrocytes at high flow rates has not been previously studied. The fabrication process we use results in roundedness of 0.5 μm for asymmetric isosceles triangular posts with 62 μm height and width. Plastic micro-molding approaches would have larger roundedness.

Increasing the roundedness of 60 μm asymmetric isosceles triangular posts from 0.5 μm to 7.5 μm results in a more than 10-fold increase in the fraction of erythrocytes displaced into the product (Figure 4.22(a)). Further increasing the roundedness to

create an extended semi-circle (Figure 4.22(a)) causes the fraction of erythrocytes displaced into the product to decrease to a level similar to that with circular posts.

The effect of the roundedness of asymmetric isosceles triangular posts on the fraction of erythrocytes displaced into the product correlates well with the asymmetry in the distribution of the centripetal acceleration of the fluid in the gap (Figure 4.22(b)). As the roundedness of the asymmetric isosceles triangular post increases from $0.5 \mu\text{m}$ to $7.5 \mu\text{m}$, the fluid accelerating around the bumping side of the post sweeps out a larger radius, causing the region of high centripetal acceleration from fluid accelerating around the bumping side of the post to extend further into the gap, while the centripetal acceleration around the non-bumping side of the post on the opposite side of the gap is limited to approximately zero. The further the region of high centripetal acceleration from fluid accelerating around the bumping side of the post extends into the gap, the more fluid is affected due to the vertical velocity profile in the gap being parabolic, which results in most of the fluid flowing near the center of the gap. We show in section 4.5.5 that the erythrocyte contamination of the product is directly related to the integral of the centripetal acceleration multiplied by the vertical velocity over the width of the gap.

Effect of Post Asymmetry and Post Roundedness on Erythrocyte Contamination of the Product

Right triangular posts and quarter-circular posts both lack left-right (about an axis parallel to the flow direction) and up-down (about an axis perpendicular to the flow direction) symmetry (Figure 4.23). However, at Re of 15, right triangular posts displace 100 times more erythrocytes into the product than quarter circular posts. Similarly, asymmetric isosceles triangular posts displace more than 100 times more erythrocytes into the product than extended semi-circular posts at Re of 15, as shown in section 4.5.4. This shows that the post asymmetry does not affect erythrocyte

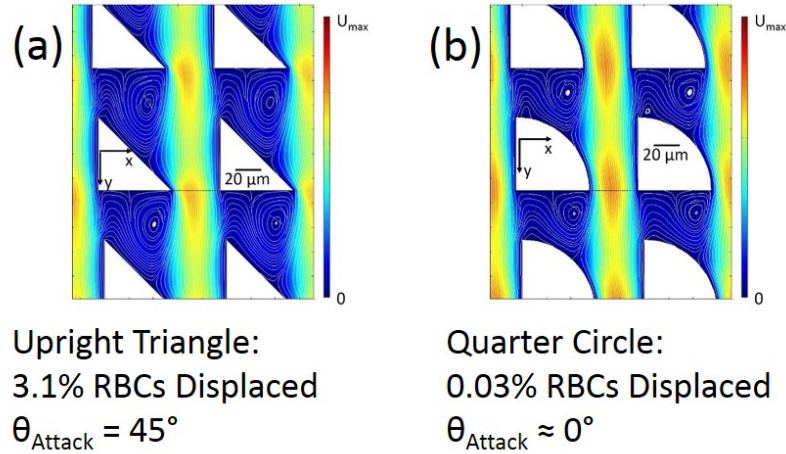


Figure 4.23: Surface plots of fluid velocity in a DLD array with $60 \mu\text{m}$ posts, $40 \mu\text{m}$ gaps, and $1/20$ tilt at Re of 20, the experimentally observed fraction of erythrocytes displaced into the product at Re of 15, and the fluid “angle of attack” for (a) right triangular posts and (b) quarter circular posts. Note that while both right triangular posts and quarter circular posts lack both left-right and up-down symmetry, right triangular posts displace 100 times more erythrocytes into the product than quarter circular posts at Re of 15.

contamination of the product at high flow rates ($\text{Re} > 1$) when the radius of curvature of the post on the upstream edge is at least half the size of the post itself. This effect can be seen in the symmetry (about an axis parallel to the flow direction through the center of the gap) of the high velocity region in the gap at Re of 20, which is asymmetric for right triangular posts but symmetric for quarter circular posts (Figure 4.23).

4.5.5 Working Model of Dependence of Undesired Erythrocyte Displacement on Post Shape at High Flow Rates (Moderate Re) and Physical Interpretation

In this section we present a method, supported by our experimental results, to predict undesirable erythrocyte displacement into the product based on post shape at high flow rates (moderate Re), a qualitative physical model that explains undesired

erythrocyte displacement based on post shape at high flow rates, and a discussion of the possible underlying physical high flow rate mechanisms that could be causing undesired erythrocyte displacement based on our experimental results.

Predictive Capability of Undesired Erythrocyte Displacement into the Product Based on Post Shape at High Flow Rates

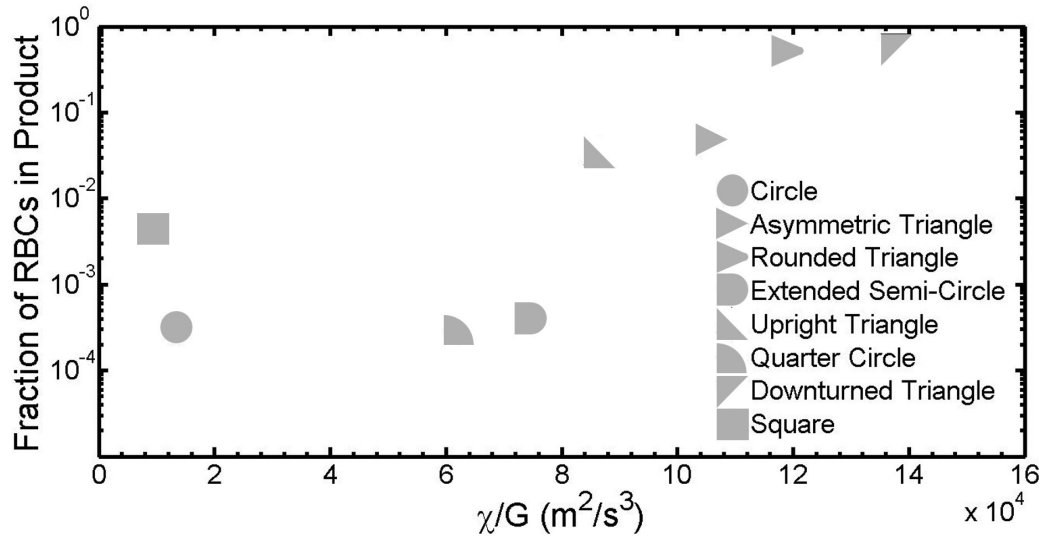


























Figure 4.24: Experimentally measured fraction of erythrocytes displaced into the product (Table 4.4) as a function of integrated centripetal acceleration times vertical velocity across the width of the gap at Re of 20. Note that the y-axis (“Fraction of RBCs in Product”) is log-scale.

In Section 4.5.4, for various post shapes, we have seen that asymmetry in the fluid centripetal acceleration distribution in the gap correlates well with erythrocyte contamination of the product at high flow rates ($Re > 1$). For symmetric post geometries, we have seen that the centripetal acceleration distribution is symmetric about the center of the gap, with a difference in sign indicating opposite curvature. For asymmetric post geometries, we have seen that the extent of erythrocyte contamination of the product is directly related to how far into the gap the high centripetal acceleration around the bumping side of the post at one side of the gap extends relative to how

Table 4.5: Experimentally measured fraction of erythrocytes displaced into the product at Re of 15 and integrated curvature times vertical velocity across the width of the gap (χ/G) at Re of 20 for the post shapes in Table 4.4.

Tilt	Post	Flow	Geometry	% RBCs in Product	χ/G (m ² /s ³)
			Asymmetric Triangle	4.9	104786.5
			Circle	0.03	13216.5
			Rounded Triangle	52.3	119080.0
			Extended Semi-Circle	0.04	74500.0
			Upright Triangle	3.1	86345.1
			Quarter Circle	0.03	62372.7
			Downturned Triangle	65.2	137814.9
			Square	0.43	9481.3

far into the gap the high centripetal acceleration around the non-bumping side of the post at the opposite side of the gap extends. The “how far into the gap” matters because little fluid travels next to the walls; most of the fluid travels near the middle of the gap, as can be seen in the vertical velocity (v_y) profiles in Figure 4.25. In order to quantify this phenomenon, we compute χ , which we define as the integral of the centripetal acceleration, a_c , times the vertical velocity through the gap, v_y across the width of the gap, G :

$$\chi = \int_0^G v_y(x) \cdot a_c(x) dx \quad (4.17)$$

Numerically, our simulations are divided into 39 streamlines through the gap. The streamlines have a spacing of 1 μm , with the first one separated from the post by 1 μm . Thus, we compute:

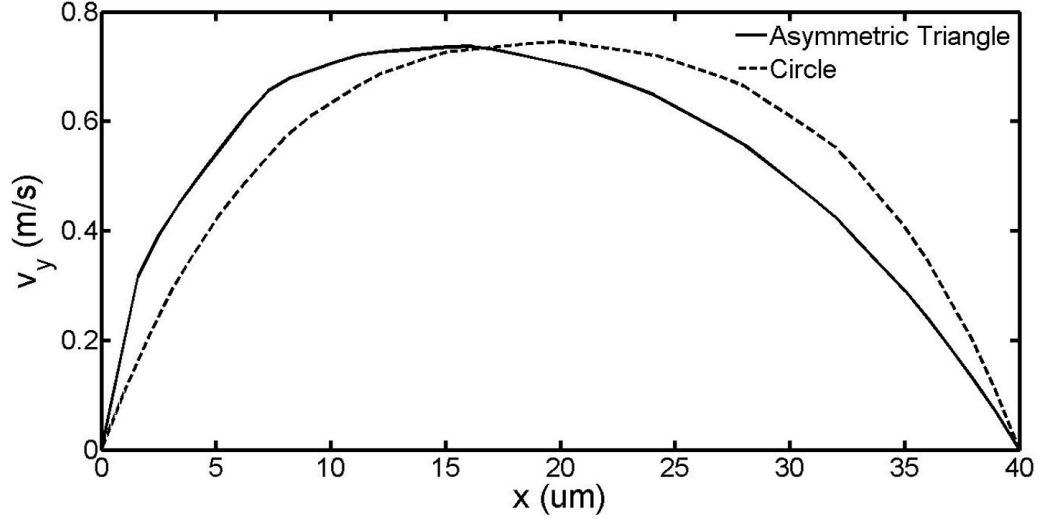


Figure 4.25: Magnitude of the vertical velocity across the width of the gap in DLD arrays with circular and asymmetric triangular posts at Re of 20. Note that the peak vertical velocity is shifted toward the bumping side of the post ($x=0 \mu\text{m}$) for asymmetric triangular posts compared to circular posts, as characterized by Louterback et al. [51].

$$\frac{\chi}{G} = \sum_{k=1}^{39} v_y(k) \cdot a_c(k) \quad (4.18)$$

For each of the eight post geometries in Table 4.4, we calculate χ/G at Re of 20 and compare to the erythrocyte contamination of the product observed experimentally (Figure 4.24 and Table 4.5). The results are striking. Except for a small deviation for the square posts, there is a monotonic relationship between χ/G and the fraction of undesired erythrocytes displaced into the product. Thus, we feel we have a strong prediction capability for undesired erythrocyte collection at high flow rates that we can use for designing new post shapes.

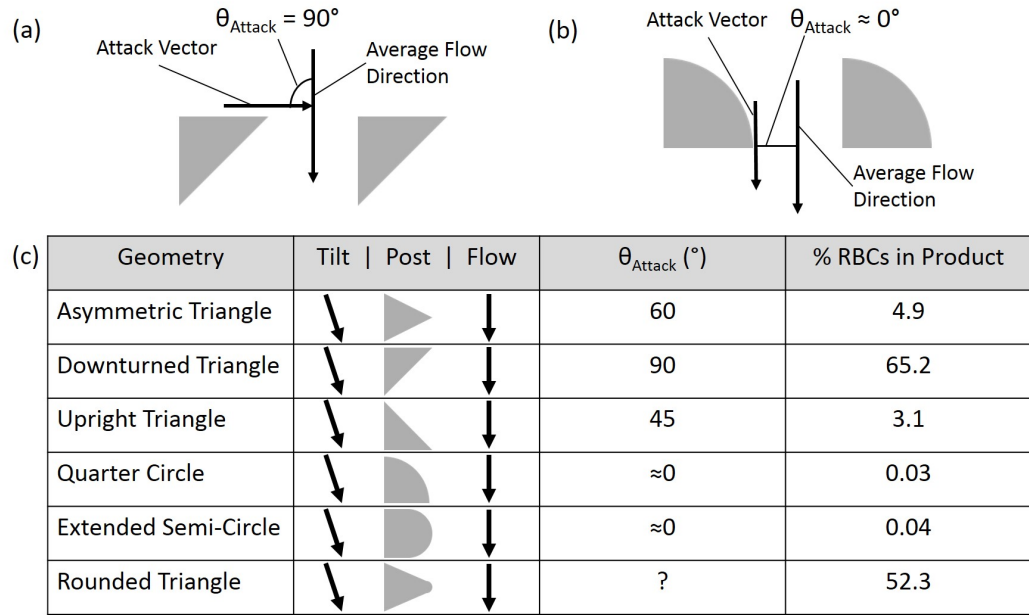


Figure 4.26: As Re increases, the “attack angle” of the leading edge of the post into the gap becomes important with respect to inertial effects. We show the attack angle of the leading edge of the post into the gap relative to the average flow direction for (a) the downturned triangle and (b) the quarter circle. (c) The “attack angle” strongly correlates with undesired erythrocyte displacement into the product at Re of 15 for asymmetric post shapes.

Qualitative Physical Model Explains Dependence of Erythrocyte Displacement at High Flow Rates on Post Shapes

The above subsection has shown a strong correlation between the asymmetry of flow curvature in the gap and undesired erythrocyte collection. We now qualitatively discuss why certain post shapes have this property.

(i) **Asymmetry:** Gaps which are symmetric do not have hydrodynamic asymmetry. Any undesired inertial effect pushing a particle one way at one side of the gap will be countered by an opposite vector at the other side of the gap. As expected, the circular and square posts both have relatively low undesired erythrocyte collection.

(ii) **Attack Angle of Leading Edge of Post Shape into the Gap:** At low Re (no inertial effects), fluid flow is reversible. Reversing the sign of the pressure gradient

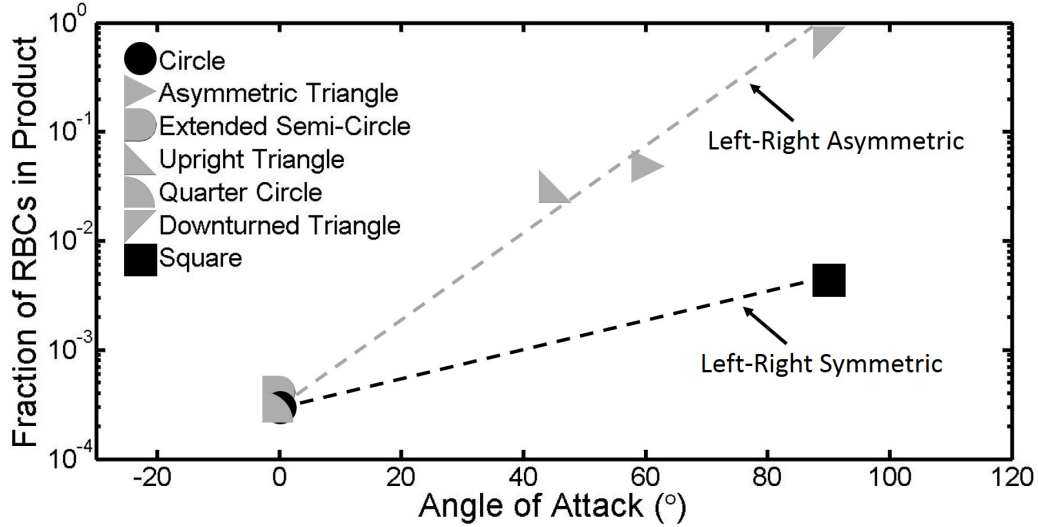


Figure 4.27: As Re increases, the “attack angle” of the leading edge of the post into the gap becomes important with respect to inertial effects. We show the attack angle of the leading edge of the post into the gap relative to the average flow direction correlates strongly with undesired erythrocyte displacement into the product for left-right asymmetric post shapes (shown in gray) and significantly less strongly with undesired erythrocyte displacement into the product for left-right symmetric post shapes (shown in black). Note that the y-axis (“Fraction of RBCs in Product”) is log-scale.

reverses the flow direction, but streamlines are unchanged. This changes at high Re . Namely, we may expect a post with a large “attack angle” going into the gap to lead to more inertial effects, since the fluid and especially particles trying to follow the fluid must undergo a larger change in direction of velocity (centripetal acceleration), as shown in Figure 4.26(a) and (b) for the cases of large and small “attack angle”, respectively.

Undesired erythrocyte displacement into the product at Re of 15 correlates well with the attack angle of the leading edge of the post into the gap for left-right asymmetric post shapes (Figure 4.26(c)). The post shape with the largest attack angle, the downturned triangle, has the largest erythrocyte displacement into the product, while the two post shapes with nearly 0° angle, the quarter circle and the extended semi-circle, have very little erythrocyte displacement into the product. For left-right

symmetric post shapes, the correlation between the attack angle of the leading edge of the post into the gap and undesired erythrocyte displacement into the product at Re of 15 is significantly weaker compared to that for left-right asymmetric post shapes (Figure 4.27). While the qualitative model gives us good physical intuition, it unfortunately cannot explain the high erythrocyte displacement by the rounded asymmetric triangle ($7.5 \mu\text{m}$ radius), even though the quantitative numerical model of the previous section can predict it.

Possible Physical Mechanisms for Undesired Erythrocyte Collection at High Flow Rates

So far, we know that the amount of fluid undergoing high centripetal acceleration into an asymmetric gap correlates well with undesired erythrocyte collection at high flow rates. We hypothesize that it is actually responsible for it.

We now discuss which of the possible mechanisms that we describe in detail in Section 4.2 could be responsible for this:

- **Inertial Lift and Dean’s Flow Forces:** The undesired erythrocyte collection is unlikely to be due to these mechanisms because the minimum flow rate required for particles (or cells) to reach stable equilibrium positions due to these forces is two orders of magnitude greater than the highest flow rates used in our experiments. This makes it highly unlikely that these forces are sufficient to cause particles to cross streamlines, resulting in displacement into the product.
- **Lift Effects from Asymmetry:** Undesired erythrocyte collection in the product output cannot be due to lift effects specific to vesicles (erythrocytes) arising from asymmetry, since the effect we observe also occurs for rigid polymer microspheres. However, effects similar to those involved in pinched-flow fractionation could be responsible for the effect we observe.

- **Centripetal Acceleration and the “Slingshot” Effect:** Undesired erythrocyte collection in the product output cannot be due to this mechanism as the displacement resulting from this mechanism is at least two orders of magnitude too small to cause erythrocyte displacement into the product, as calculated in Section 4.5.3.
- **Erythrocyte Reorientation (Flipping):** It cannot be due to this mechanism because the flow-rate dependent displacement into the product is observed for rigid polymer microsphere beads below the critical size of the array as well as erythrocytes (Section 4.5.1), indicating that this effect is not due to reorientation of the erythrocytes or other specific, flow-dependent behavior of erythrocytes.

Thus, we conclude that effects similar to those involved in pinched-flow fractionation are responsible for erythrocyte displacement into the product at high flow rates for asymmetric post shapes. Pinched flow fractionation has been extensively characterized experimentally [66, 80, 86], but the fundamental mechanisms are not well understood.

This work has focused on arrays with shallow tilt angles ($\text{tilt} < 1/20$), which are common in applications involving separation of nucleated cells from blood due to the large size range of the target cells. In arrays with steeper tilt angles, symmetric post geometries can cause an asymmetric centripetal acceleration distribution in the gap, resulting in displacement of particles below the critical size of the array at high flow rates. Results by Y.S. Lubbersen et al. [56, 54] show that this occurs for circular and quadrilateral posts with tilt angles of $1/6$ and $1/4$, respectively, as Re is increased from 2 to 30. One possible solution to this undesirable effect is to use asymmetric posts to compensate for hydrodynamic asymmetry arising from the tilt angle of the array in these cases.

Future work will probably need combined fluid and particle modelling of the flow. Calculation of the flow pattern with no particles and predicting particle behavior



















from this flow profile is likely not sufficient for further work, since high flow velocity hydrodynamic lift effects depend on the effect of the particle on the flow pattern.

4.6 Optimal Post Geometry for High-Throughput Separation of Nucleated Cells from Blood with Minimal Erythrocyte Contamination

The optimal post geometry for high-throughput separation of nucleated cells from blood has two characteristics: (1) high nucleated cell (leukocyte) collection efficiency and (2) low collection efficiency of undesired erythrocytes. Section 4.4 showed (1) requires minimum shear at the post surface against which the cell can be compressed and is achieved using post shapes that have a vertex pointing into the gap in the bumping direction. Section 4.5 showed (2) requires that the flow in the gap have a symmetric centripetal acceleration distribution and is satisfied by using post shapes with symmetry about the axis parallel to the flow direction.

Section 4.4 described leukocyte collection at Re of 2.3, corresponding to an undiluted blood flow rate of $100 \mu\text{L}/\text{min}$ and processing of an undiluted blood volume of 3 to 4 mL for different post shapes. We now report the undesired erythrocyte collection at the product output in these experiments. The results are shown in Table 4.6 and plotted in Figure 4.28, with leukocyte yield (harvested into the central product outlet) on the y-axis and erythrocyte fraction in the product output on the x-axis. Consistent with our results in the previous section, post shapes that are symmetric about an axis parallel to the flow direction result in relatively low erythrocyte displacement into the product compared to post shapes that are asymmetric about this axis (Figure 4.28). There is a 130-fold increase in erythrocyte displacement into the product between asymmetric triangular posts and circular posts, whereas the difference in erythrocyte

Table 4.6: Leukocyte yield (harvested into the central product outlet) and erythrocyte fraction in the product output for different post geometries under the same experimental conditions. Array parameters are $19\ \mu\text{m}$ posts, $17\ \mu\text{m}$ gaps, and $1/42$ tilt for all post geometries except the asymmetric triangle, which has $34\ \mu\text{m}$ posts, $22.5\ \mu\text{m}$ gaps, and $1/42$ tilt. The average flow velocity in the gap is $13.5\ \text{cm/s}$, the Reynolds number is 2.3, and the average shear rate is $15000\ \text{s}^{-1}$ for all post geometries. Volume of blood was greater than 3 mL for each post shape, and blood was diluted 1:4. The running time ranged from 30 to 40 minutes for each post shape.

Tilt	Post	Flow	Geometry	% WBCs in Product	% RBCs in Product
			Asymmetric Triangle	81.3	1.158
			Circle	25.2	0.009
			Quarter Circle	18.7	0.011
			Rhombus	32.9	0.015
			Symmetric Triangle	64.8	0.038
			Diamond	83.6	0.009

displacement into the product between symmetric triangular posts and circular posts is only 4-fold.

For most post shapes, one can achieve high leukocyte yield or low erythrocyte contamination, but not both. Fortunately, diamond posts simultaneously achieve a high ($>80\%$) fraction of leukocytes displaced into the product with a low level of erythrocyte displacement into the product comparable to that achieved with circular posts ($<0.02\%$).

Combining high-throughput operation of DLD arrays with inhibition of clot formation, we separate leukocytes from 3.7 mL of whole blood in less than 45 minutes using a single DLD array with diamond posts. The leukocyte capture rate is 83%, which is the highest reported in a DLD array in which the average shear rate exceeds $10,000\ \text{s}^{-1}$. Erythrocyte concentration in the product is $3 \times 10^4\ \text{mL}^{-1}$, representing a depletion by a factor of more than 10,000 relative to the starting sample. Altogether,

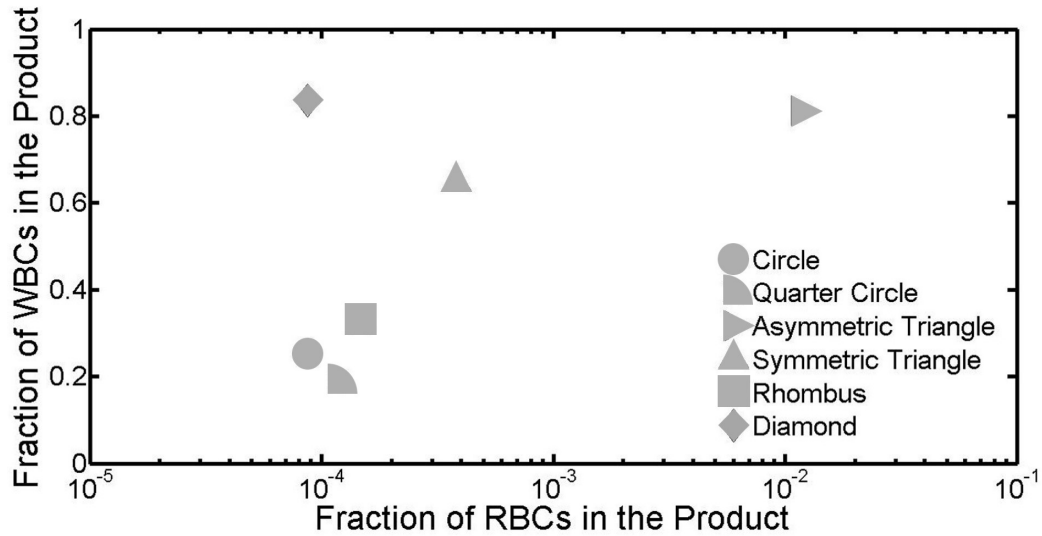


Figure 4.28: Fraction of leukocytes in the product versus fraction of erythrocytes in the product for six different DLD array post geometries at Re of 2.3. Note that the x-axis (Fraction of RBCs in the Product) is log-scale. The shape of the posts is schematically indicated, assuming the flow direction is vertical. The tilt of the array is to the right as one moves down through the array, and the flow direction is from top to bottom.

this represents the highest efficiency separation of leukocytes from the largest volume of blood in the shortest time ever achieved using DLD arrays. For comparison, in the largest scale separation of leukocytes from whole blood previously reported, D. Inglis et al. processed undiluted blood at a rate of $4 \mu\text{L}/\text{min}$ (1/20 as fast as we report in terms of undiluted blood flow rate) per DLD array, separating 98% of leukocytes from $80 \mu\text{L}$ of blood with more than 100 times the erythrocyte contamination of the product that we report here [37].

4.7 Conclusion

Shear-induced cell deformation and potential inertial effects arising from Re increasing above 1 present two major limitations to high-throughput separation of nucleated cells from whole blood using DLD arrays. In this chapter, we show:

(i) The extent of shear-induced cell deformation is proportional to the shear rate of the fluid bending around the surface of the micro-post against which the cell can be compressed. It can be minimized by using post geometries with vertices pointing into the gap in the bumping direction.

(ii) The displacement of erythrocytes into the product at high flow rates for certain micro-post geometries correlates well with asymmetry in the centripetal acceleration distribution in the gap between the micro-posts and can be minimized by using post shapes with symmetry about an axis parallel to the flow direction.

We then show that diamond micro-posts overcome both these limitations, simultaneously achieving maximum displacement of leukocytes into the product while minimizing erythrocyte displacement into the product.

Using this approach, we have demonstrated that 83% of leukocytes can be separated from ~ 4 mL of whole blood in less than 45 minutes with a single DLD array with diamond posts, resulting in a product with 10,000-fold depletion of erythrocytes relative to the starting blood sample. Standard micro-fabrication techniques have been previously used to produce a chip containing 15 DLD arrays in parallel, which would require an area of 36 mm by 70 mm for the array presented in this paper [40, 36]. Combining a chip containing 15 of our DLD arrays in parallel with the advances presented in this chapter should allow for high-efficiency separation of leukocytes from over 50 mL of blood in less than one hour.

Chapter 5

Controlling Anisotropic Conduction in DLD Arrays with Post Geometry at Low Reynolds Number

5.1 Introduction

The performance of deterministic lateral displacement (DLD) arrays in separating particles based on size can be enhanced or diminished by misalignment of the pressure gradient to the average flow direction due to anisotropic conduction. This misalignment of the pressure gradient to the average flow direction has been shown to create a third type of particle behavior, mixed motion, which results in particles in an intermediate size range traveling at an angle between the average flow direction and the array tilt angle for an array with circular posts. In this chapter, we show (i) how post geometry and tilt angle affect this misalignment of the pressure gradient and (ii) how increasing the spacing between rows in the direction of the flow minimizes

the effect of post geometry on anisotropic conduction. We then present a practical application of using the misaligned pressure gradient to adjust the critical size of the DLD array.

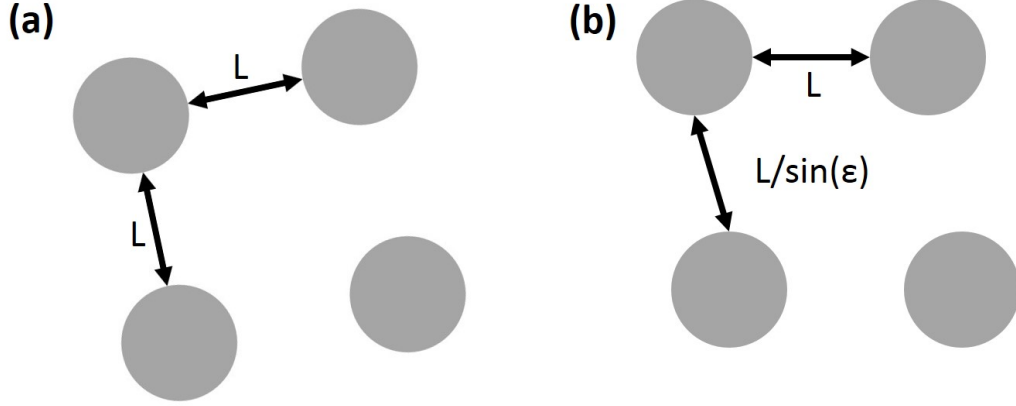


Figure 5.1: (a) A tilted square unit cell array with gap size L and tilt angle (ϵ) of $1/5$. (b) A rhombic unit cell array with gap size L and tilt angle (ϵ) of $1/5$. Array is oriented such that the average flow direction is vertical, from top to bottom.

Although the original DLD array designed by L.R. Huang et al. used an array with a tilted square unit cell [30], rhombic unit cell arrays have become more widely used since rhombic unit cell arrays allow for placing multiple arrays in series with varying critical sizes (Figure 5.1). In a rhombic array, the rows are perpendicular to the average flow direction while the columns are parallel to the tilt angle. This results in anisotropic conduction, in which the conductivity in the direction of the flow is less than the conductivity in the direction perpendicular to the flow by an amount dependent upon the tilt angle of the array. In contrast, a DLD array with a tilted square unit cell is expected to be an isotropic conductor with fixed conductivity at any angle. However, we show in Section 5.2 that this is only the case for certain post shapes.

A fundamental assumption of the theory that characterizes the critical size for DLD arrays is that the average fluid flow is at a fixed angle to the post lattice that forms the array [35]. Previous work in minimizing the discrepancy between the

anisotropic conduction of rhombic DLD arrays with this fundamental assumption has focused primarily on two areas. First, D. Inglis devised a method for designing the boundaries of DLD arrays to ensure vertical flow by causing one streamline to shift opposite the tilt direction with each subsequent row in the direction of the flow [34]. Second, T. Kulrattanakarak et al. showed that anisotropy of the array causes particles in an intermediate size range to travel at an angle in between the average flow direction and the tilt angle [43, 44]. This effect is similar to the multidirectional sorting modes with DLD arrays achieved by B.R. Long et al. by using rational number (N/M , where N and M are both integers) tilt angles [48].

Recently, post shape engineering in DLD arrays has emerged as a way to increase throughput [49, 50], sort non-spherical particles [88, 70, 39], and reduce the shear experienced by cells traveling through the array [1]. However, this recent work has focused on operation of DLD arrays at $Re > 1$. In this chapter, we focus on the effect of post shape on anisotropic conduction in the array at $Re \sim 0.01$ and how post geometry can be used to achieve a different effective critical size for the same array parameters.

More recently, anisotropic conduction in the array has been used to enhance separation efficiency and throughput. K.K. Zeming et al. have adjusted the ratio of the spacing between the rows in the direction of the flow to the gap size in order to enhance the throughput and separation efficiency of erythrocytes [89]. This work built on previous work showing that a single line of obstacles tilted at an angle to the average flow direction is sufficient to concentrate particles based on size from sufficiently dilute suspensions of particles [55, 16]. This allows for scaling of the fluidic resistance of the array based on the starting concentration (particles/volume) of particles in the suspension from which concentration is desired.

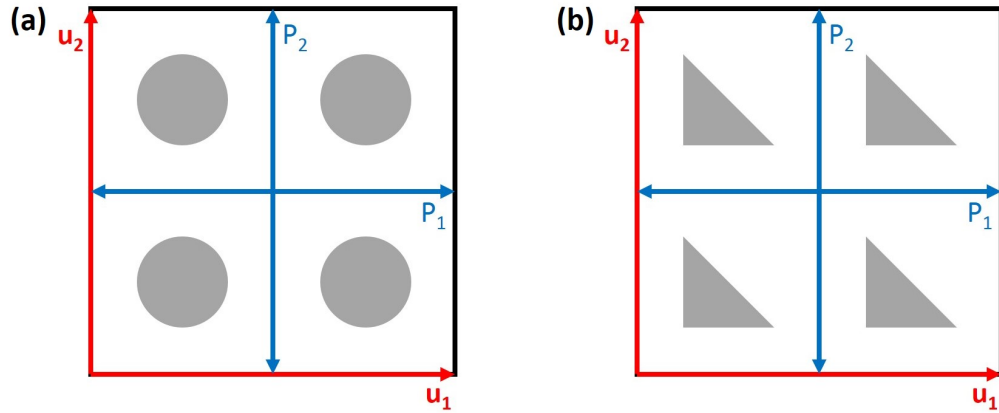


Figure 5.2: (a) A square array of circular posts is an isotropic conductor. Flow along axis \mathbf{u}_1 is driven by a pressure difference P_1 and will not generate a pressure difference P_2 along axis \mathbf{u}_2 . (b) Square array of upright asymmetric triangular posts is an anisotropic conductor. It is observed in simulation that a flow along axis \mathbf{u}_1 , driven by a pressure difference P_1 , generates a pressure difference P_2 along axis \mathbf{u}_2 .

5.2 Anisotropic Conduction

The difference between isotropic fluid conduction and anisotropic fluid conduction in an array of square posts is demonstrated in Figure 5.2. Figure 5.2(a) shows a square array of circular posts, which has been verified in simulation (details below) to be an isotropic conductor. This means that a flow along axis \mathbf{u}_1 is driven by a pressure differential P_1 in the \mathbf{u}_1 direction and will not generate a pressure differential P_2 in the direction of axis \mathbf{u}_2 . Figure 5.2(b) shows a square array of upright asymmetric triangular posts, which has been observed in simulation as an anisotropic conductor. This means that a flow along axis \mathbf{u}_1 driven by a pressure differential P_1 in the \mathbf{u}_1 direction will generate a pressure differential P_2 in the direction of axis \mathbf{u}_2 . For a flow along axis \mathbf{u}_1 , the ratio P_2/P_1 can be used as a measure of anisotropic conduction.

In a standard DLD array, a pressure is applied to drive the flow in a given direction (vertical in this case). Since there can be no flux through the horizontal side walls, if the array design is that of an anisotropic conductor, an internal pressure gradient will develop to keep the flow vertical. This internal pressure gradient can be used to

characterize the anisotropic conduction of the array. This is analogous to the Hall effect in semiconductors.

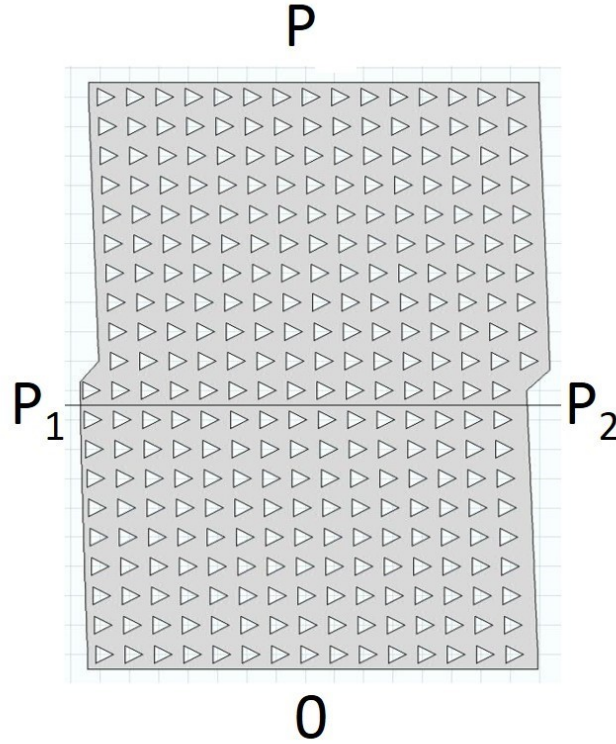










Figure 5.3: Schematic of simulation used to characterize anisotropic conduction in the DLD array with rhombic unit cell. A uniform pressure, P , is applied across the top of the array, and the bottom of the array is maintained at a uniform pressure of 0. This pressure differential drives the flow through the array, which is 20 rows long and 15 columns wide. The transverse pressure gradient, $\Delta P = P_2 - P_1$, is calculated from the difference between the pressures measured at the right and left walls of the array along the line through the middle of the array above. The array shown here has $60 \mu\text{m}$ triangular posts, $40 \mu\text{m}$ gaps, and $1/20$ tilt. The walls are designed to ensure vertical flow at the sides of the array [34].

The array used in our simulations is 20 rows long and 15 columns wide (Figure 5.3). It is a “rhombus” array (not a tilted square array), and the rhombus shape alone introduces a fluid flow anisotropy, which is dependent upon the tilt angle of the array. In the next section, we investigate the effect of post shape on anisotropic conduction at different array tilt angles. The posts we use can be inscribed within a square with

Table 5.1: Post geometries for which the transverse pressure generated by a pressure gradient in the direction of the flow is measured. All post shapes can be fit within a square with side length $60 \mu\text{m}$. Flow direction is from top to bottom with respect to post shape in the table.

Post Shape	Geometry
	Circle
	Right Up-Down Symmetric Triangle
	Left Up-Down Symmetric Triangle
	Upright Asymmetric Triangle
	Downturned Asymmetric Triangle
	Diamond
	Square
	Left-Right Symmetric Triangle

side $60 \mu\text{m}$, the gap is $40 \mu\text{m}$, and the tilt is varied between $1/5$ and $1/50$. The array unit cell is rhombic and the walls are designed using the method by D. Inglis to ensure vertical flow near the edges of the array [34]. Simulations are performed using the COMSOL 2D laminar flow module at $\text{Re} \sim 0.01$ by applying a pressure P of 1 Pa at the top boundary of the array. No-slip boundary conditions along the walls of the array and the edges of the posts are applied. The transverse pressure, $\Delta P = P_2 - P_1$, is then calculated in the simulation to characterize the anisotropic conduction in the DLD array. The post geometries we examine in this chapter are shown in Table 5.1.

5.3 Effect of Post Shape and Tilt Angle on Transverse Pressure Gradient

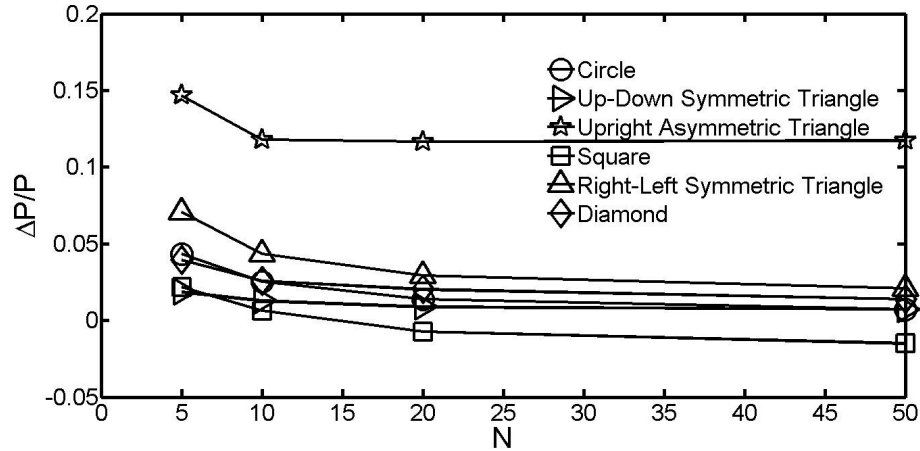


Figure 5.4: Relative transverse pressure gradient ($\Delta P/P$) as a function of tilt angle (tilt angle is $1/N$) for six different post geometries in a DLD array with a rhombic unit cell. The simulation is performed at $\text{Re} \sim 0.01$ for all post geometries tested. Note that the relative transverse pressure gradient remains significant even for large N for the upright asymmetric triangle but decreases to very small values at large N for the other five post geometries.

The effect of tilt angle on the transverse pressure gradient was measured for six different post shapes (Figure 5.4). All of the post shapes are sized such that the post shapes can fit within a square with side length of $60 \mu\text{m}$.

The transverse pressure gradient decreases with increasing N (increasingly shallow tilt angles) for all six post shapes. Note that at large N , there is very little tilt, the rhombic unit cell is approximately square, and the differences in the relative transverse pressure gradient (measure of anisotropic conduction in the DLD array) are primarily a function of post shape. Circular posts at large N approach the square array of Figure 5.2(a) and thus have no anisotropic effects.

We expect post shapes with symmetry about axes parallel and perpendicular to the average flow direction (circle, diamond, square) to have little anisotropic effects based on shape. A single qualitative view might expect a triangular post with a vertex pointing into the gap on one side to cause anisotropic conduction, but this is contradicted by the up-down symmetric triangle. At present, there is no intuitive understanding about why the upright asymmetric triangular post shape causes such a large anisotropic effect.

In order to better understand why the upright asymmetric triangular post shape causes such a large anisotropic effect, we examine four triangular post shapes that lack symmetry about at least one axis (Figure 5.5). Two of these post shapes have up-down symmetry but lack left-right symmetry (right and left up-down symmetric triangles), while the other two lack both left-right and up-down symmetry (upright and downturned asymmetric triangles). Both the right and left up-down symmetric triangular post shapes have transverse pressure gradients that decrease with increasing N , and the direction of the transverse pressure gradient is not sensitive to the orientation of the post shape in these two cases. For the upright and downturned asymmetric triangular post shapes, the transverse pressure gradient remains significant even at large N , and the direction of the transverse pressure gradient is sensitive

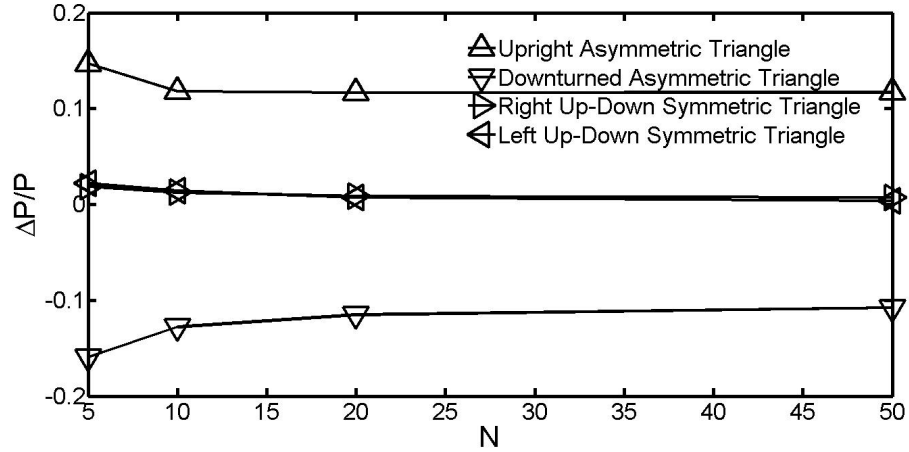


Figure 5.5: Relative transverse pressure gradient ($\Delta P/P$) as a function of tilt angle (tilt angle is $1/N$) for four asymmetric triangular post geometries in a DLD array with a rhombic unit cell. The simulation is performed at $Re \sim 0.01$ for all post geometries tested. Note that the relative transverse pressure gradient remains significant even for large N for the upright and downturned asymmetric triangular post shapes but decreases to very small values at large N for the up-down symmetric triangular post shapes. Also, note that the direction of the transverse pressure gradient is sensitive to the orientation of the up-down asymmetric post shapes but not the up-down symmetric post shapes.

to the orientation of the post shape, as indicated by the opposite sign of the transverse pressure gradient for the downturned asymmetric triangle compared to the upright asymmetric triangle. We next examine the effect of spacing of the rows in the direction of the flow on the transverse pressure gradient with upright and downturned asymmetric triangular post shapes in order to better understand why these two post shapes cause such a large anisotropic effect.

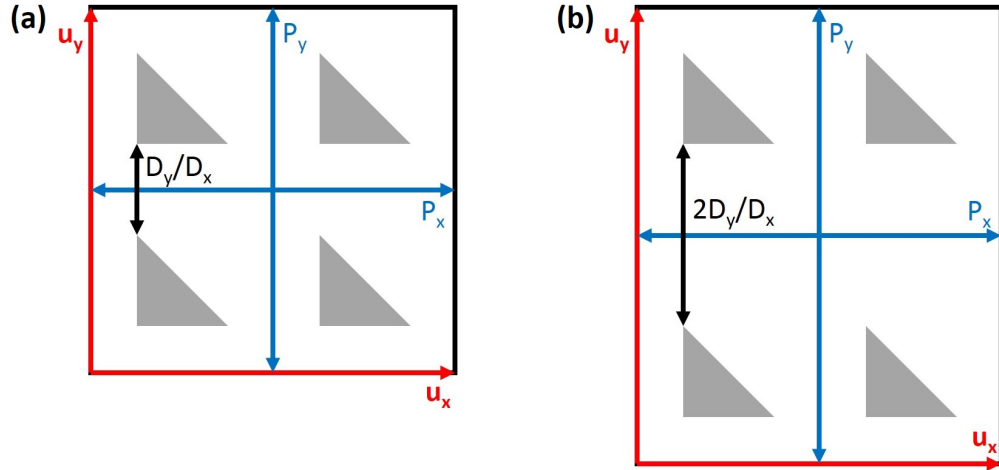


Figure 5.6: (a) Square array of upright asymmetric triangular posts is an anisotropic conductor. It is observed in simulation that a flow along axis \mathbf{u}_y , driven by a pressure difference P_y , generates a pressure difference P_x along axis \mathbf{u}_x . (b) We examine the effect of doubling (and tripling, not shown) the spacing between rows, D_y/D_x , on the pressure difference P_x along the axis \mathbf{u}_x generated by a flow along the axis \mathbf{u}_y , which is driven by a pressure difference P_y .

5.4 Effect of Spacing between Rows on Transverse Pressure Gradient for Different Post Geometries

We have established that post shape contributes to anisotropic conduction in DLD arrays even if the tilt angle is shallow. In this section, we examine how spacing within the array can be used to minimize anisotropic conduction. We cannot modify the gap size without changing the critical size of the array [35]. Therefore, we examine how we can change the spacing between rows in the direction of the flow to minimize anisotropic conduction.

In Figure 5.6(a), we show the standard array, with unit size gap and D_y/D_x spacing between the rows. The fluidic resistance R_y for fluid flowing along u_y is fixed by the gap. However, the fluidic resistance R_x for fluid flowing along u_x can be significantly

reduced by increasing the spacing of the \mathbf{u}_x rows along the \mathbf{u}_y axis. Figure 5.6(b) shows the array with this spacing doubled compared to the array in Figure 5.6(a). Thus, if applying a vertical (along \mathbf{u}_y axis) pressure gradient causes a flow component in the \mathbf{u}_x direction, only a very small pressure gradient in the \mathbf{u}_x direction is needed to induce a flow to counterbalance this, leading to a small P_x/P_y .

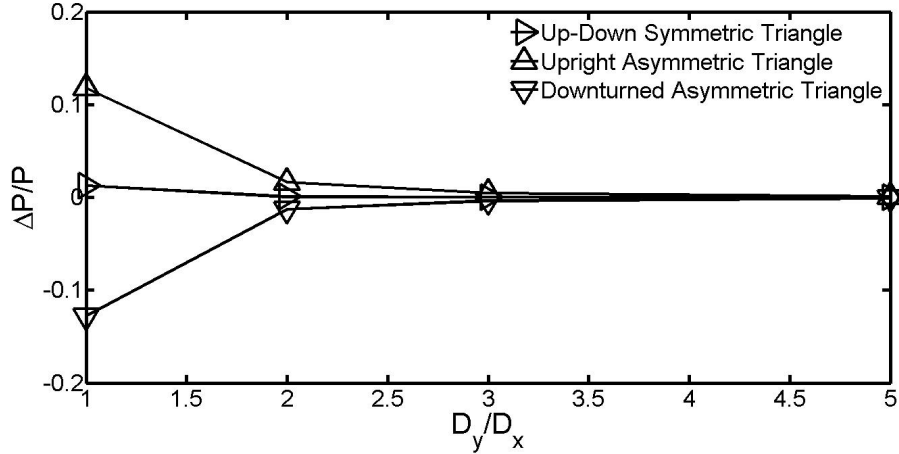


Figure 5.7: The relative transverse pressure gradient ($\Delta P/P$) was measured as the spacing between rows in the direction of the flow (D_y) was increased relative to the gap (D_x) for three post geometries in a DLD array with tilt $1/10$. Although upright and downturned asymmetric triangles have significantly larger relative transverse pressure gradients compared to up-down symmetric triangles when the row spacing in the direction of the flow is equal to the gap, this difference decreases rapidly as the spacing between rows of posts in the direction of the flow increases relative to the gap size.

Thus, the effect of post shape on the transverse pressure gradient is highly dependent on the spacing of the rows of posts in the direction of the flow (D_y) relative to the gap between posts in the direction perpendicular to the flow (D_x). We simulate the transverse pressure gradient as a function of D_y/D_x for the upright asymmetric triangle, downturned asymmetric triangle, and up-down symmetric triangle (Figure 5.7). Simply doubling D_y/D_x causes the transverse pressure gradient to decrease by more than a factor of 7 for the upright and downturned asymmetric triangular posts. Increasing D_y/D_x to 3 almost completely removes all anisotropic conduction effects.

This shows that the transverse pressure gradient is sensitive to the transverse fluidic resistance (R_x), since R_x decreases by a factor of 4 when D_y/D_x is doubled and by a factor of 9 when D_y/D_x is tripled.

5.5 Conclusion

Anisotropic conduction in DLD arrays, which causes a misalignment of the pressure gradient to the average flow direction, can be caused by either a rhombic (not tilted square) unit cell array or by post shapes which are asymmetric. For a grid with approximately equal spacing in the x and y directions, this misaligned pressure gradient is minimized by post shapes that are symmetric about axes parallel and perpendicular to the average flow direction. For arrays with a tilt angle achieved with a rhombic unit cell array, as is commonly used in DLD arrays, a transverse (perpendicular to the average flow direction) pressure develops between the sidewalls of the array in order to keep the average flow direction straight, since there can be no fluid flux into the sidewalls. The magnitude of this transverse pressure is determined by the steepness of the tilt of the array and the asymmetry of the post shape, and a significant transverse pressure can cause deviations in particle behavior in the array from what would be expected by conventional DLD array theory. The magnitude of this transverse pressure is highly sensitive to the spacing of the rows in the average flow direction, and increasing (doubling or tripling) this spacing for arrays with steep tilt angles or asymmetric post shapes can reduce the magnitude of this transverse pressure to very small values.

Chapter 6

Conclusion

6.1 Summary

Deterministic lateral displacement (DLD) arrays have been used to fractionate blood into leukocytes, erythrocytes, and platelets, based on hydrodynamic size [14]. Compared to other microfluidic cell sorting technologies, DLD arrays allow for separation of nucleated cells without the background of erythrocytes, platelets, and smaller non-target cells and without requiring significant ($>5X$) dilution of the blood for operation. DLD arrays have been applied to separation of a variety of cancer cells [50, 47], malignant lymphocytes [36], and fetal nucleated erythrocytes [32] from blood. However, the volume involved in these applications has been limited to less than $100 \mu\text{L}$ due to volume-dependent performance degradation and processing time constraints. In this thesis, we presented three approaches toward improving the volume of blood that can be processed in a given time within a fixed chip area.

In Chapter 2, we made improvements to the device fabrication processes and experimental setup to allow processing of large volumes of fluid in shorter time periods. We presented three fabrication processes that increased the number of DLD arrays that could fit in a given area on a silicon chip by a factor of four. Two of these three

fabrication processes allowed a 2.5-fold increase in the maximum depth to which the DLD array could be etched, resulting in a 10-fold increase in the volumetric flow rate for a given pressure differential over that which was achievable with previous fabrication processes. We also introduced a bubble-free design of the high-throughput manifold, through which fluidic connections are made to the DLD array, removing another barrier to reliable operation of DLD arrays over longer time periods.

In Chapter 3, we identified that volume-dependent performance degradation in processing blood with DLD arrays occurs due to conventional platelet-driven clot formation. We showed the activity of calcium ions and thrombin are the dominant mechanisms driving clot formation in the DLD array and presented a method using the calcium-chelating anti-coagulant, EDTA, and the direct thrombin inhibitor, PPACK, to completely inhibit clot formation in silicon DLD arrays. We then demonstrated, using this method, capture of 86% of PC3 cancer cells from 14 mL of blood in less than 38 minutes with only 0.03% of erythrocytes contaminating the product using a single DLD array. Putting 10 DLD arrays in parallel on a chip, which is easily technically achievable [40], would allow processing of >100 mL of blood using a single chip. Previously, single DLD arrays were limited to processing less than 250 μL of blood.

In Chapter 4, we explored the effects of post shape on the behavior of leukocytes and erythrocytes at high flow rates (moderate Re). We showed that the extent of cell deformation against the micro-posts is directly related to the shear at the surface of the post resulting from fluid bending around the post and can be minimized by using post shapes that have vertices pointing into the gap. We also identified flow velocity-dependent erythrocyte contamination of the product with asymmetric triangular posts but not circular posts. We showed that the extent of this flow velocity-dependent erythrocyte displacement is directly related to asymmetry in the fluid centripetal acceleration distribution in the gap and that this flow velocity-dependent

erythrocyte displacement does not occur for post shapes for which the fluid centripetal acceleration distribution in the gap is sufficiently symmetric. This enabled, for the first time, harvesting of leukocytes from blood at a high flow rate (100 $\mu\text{L}/\text{minute}$ undiluted blood flow rate), requiring shear rate greater than $10,000 \text{ s}^{-1}$ and Re of 2.3, with both high leukocyte yield (83%) and low erythrocyte contamination ($<0.02\%$).

In Chapter 5, we examine the effect of post shape on anisotropic conduction at low Reynolds number. Anisotropic conduction occurs in DLD arrays with a parallelogram unit cell instead of a rotated square unit cell and leads to a pressure gradient that is misaligned to the average flow direction. This causes particles in a certain size range to migrate at an angle between the average flow direction and the tilt angle of the array and can potentially be used to adjust the critical size of the array for a given set of array parameters. We examine how the tilt angle of the array contributes to anisotropic conduction, show that the lateral (perpendicular to the average flow direction) velocity induced by different post shapes is the dominant contributor to anisotropic conduction at a given tilt angle, and demonstrate that increasing the spacing of the rows in the flow direction significantly reduces the misaligned pressure gradient for a given post shape.

6.2 Future Work

Widespread use of DLD arrays for therapeutic and diagnostic applications in medicine will require fabrication of DLD arrays in low-cost, disposable materials. Recently, R.S. Powell et al. have devised a method to fabricate thermoplastic DLD arrays using low-cost, regulatory-approved materials and biocompatible methods [62]. Future work could include combining the method we presented for inhibition of clot formation with use of these thermoplastic DLD arrays to experimentally measure thermoplastic DLD array performance for large volumes of blood. Decreases in device performance

compared to silicon DLD arrays could be compensated through stacking and parallelization of DLD arrays, which should be easier with thermoplastics than with silicon due to the ease with which thermoplastics can be bonded together.

The advances presented in this thesis overcome two major limitations toward separation of large cells from large volumes of blood in short times. These advances may allow pursuit of two interesting applications. First, umbilical cord blood, which is typically collected in volumes of approximately 100 mL, provides a rich source of hematopoietic (blood-forming) stem cells (HSCs) that can be used for treatment of a wide variety of diseases, including a variety of cancers, bone marrow failure syndromes, immunodeficiencies, and metabolic disorders. DLD arrays provide greater separation efficiencies and superior erythrocyte depletion compared to current state-of-the-art technology [75]. Future work would include experiments to characterize DLD array performance for separation of HSCs from cord blood samples instead of using leukocyte separation from adult peripheral blood as a model system. Second, we demonstrate that DLD arrays can be used to separate cancer cells from larger volumes and with greater separation efficiency than the U.S. Food and Drug Administration-approved CellSearch system [71]. Future work would include experiments using primary cancer cells, instead of cell lines, and development of a system for on-chip detection of small numbers of cancer cells for high-sensitivity diagnostic applications.

On-chip processing of blood offers the advantages of more precise control of reaction time and lower required quantities of reagents. Recently, high-quality on-chip washing of leukocytes for diagnostic applications [9] and on-chip lysis of leukocytes for analytical applications [10] using DLD arrays were demonstrated. Future work that may be enabled by the advances presented in this thesis would include extensions of such applications to rare cells, which would require processing large volumes of blood in short times.

Appendix A

Publications and Presentations

A.1 Peer-Reviewed Publications

- **J D'Silva**, K Louterback, RH Austin, and JC Sturm. Controlling Anisotropic Conduction in DLD Arrays with Post Geometry at Low Reynolds Number. (in preparation)
- **J D'Silva**, RH Austin, and JC Sturm. Post Geometry Design for High-Throughput Harvesting of Nucleated Cells from Blood with Minimal Erythrocyte Contamination Using Deterministic Lateral Displacement Arrays. (in preparation)
- **J D'Silva**, RH Austin, and JC Sturm. Inhibition of Clot Formation in Deterministic Lateral Displacement Arrays for Processing Large Volumes of Blood for Rare Cell Capture. *Lab on a Chip*, 15(10):2240-2247, 2015.
- Y Chen, **J D'Silva**, RH Austin, and JC Sturm. Microfluidic Chemical Processing with On-Chip Washing by Deterministic Lateral Displacement Arrays with Separator Walls. *Biomicrofluidics*, 9(5):054105, 2015.

- K Loutherbach, **J D'Silva**, L Liu, A Wu, RH Austin, and JC Sturm. Deterministic Separation of Cancer Cells from Blood at 10 mL/min. *AIP Advances* 2(4):042107, 2012.

A.2 Conference Presentations

- **CYTO 2016**, Seattle, WA. – Microfluidic Post Geometry Design for High-Throughput (100 μ L/min) Harvesting of Leukocytes from Blood using Deterministic Lateral Displacement Arrays. (talk, accepted)
- **MRS Spring Meeting 2014**, San Francisco, CA. – Microfluidic Cell Sorters for Rapid Isolation of Circulating Tumor Cells from Large Volumes of Blood. (talk)
- **MRS Spring Meeting 2013**, San Francisco, CA. – High-Throughput, High-Enrichment Microfluidic Cell Sorters for Capture of Circulating Tumor Cells from Whole Blood. (poster)
- **APS March Meeting 2013**, Baltimore, MD. – Minimizing Platelet Activation-Induced Clogging in Deterministic Lateral Displacement Arrays for High-Throughput Capture of Circulating Tumor Cells. (talk)

Appendix B

Backside Alignment Fabrication Process

This appendix details the steps in the backside alignment fabrication process described in Chapter 2 Section 2.2.2. Devices are fabricated on double-side-polished 100-mm-diameter, 550- μm -thick silicon wafers.

Front-Side Processing

1. Dehydration bake the wafer for 2 minutes at 95°C.
2. Spray on HMDS and spin immediately using recipe 3.
3. Apply ~ 3 mL AZ 4330 photoresist using a plastic transfer pipette and spin using recipe 3.
4. Soft bake at 95°C for 3 minutes.
5. Expose for 1 minute using Channel 2 on the MA6 mask aligner with hard contact setting.
6. Wait 10 minutes.

7. Develop using AZ 300 MIF developer. Development usually takes 2.5 minutes, but this can vary depending on conditions such as how long the photoresist has been outside the refrigerator and room humidity.
8. Inspect under microscope to ensure features are completely developed.
9. Etch with recipe 3 (200 μm trench etch) on the Samco 800 for 120 cycles (1 cycle \approx 1.3 μm if different etch depth is desired).

Back-Side Processing

1. To prevent scratching of features that have been etched into the front side of wafer from photoresist on the hot plate, place a clean stainless steel plate on top of the hot plate and allow temperature to reach 95°C. Flat stainless steel plates can be ordered from McMaster Carr.
2. Dehydration bake the wafer for 2 minutes at 95°C.
3. Mount in specially designed spinner chuck that prevents the front side of the wafer from touching the surface of the chuck. This specially designed chuck consists of a circular stainless steel plate that has been machined on both sides. On the front side, three metal rods protrude from the surface near the edge of the plate, spaced 120° apart, at a radius that allows for a standard 4" wafer to be placed with a flat against one metal rod and the edges of the wafer flush against the other two metal rods. This allows for rotation of the wafer with the chuck. O-rings are placed on the metal rods against the surface of the chuck, and the wafer is placed on top of the O-rings such that the front side of the wafer does not touch the chuck. The bottom of the stainless steel plate has a region cut out that allows the plate to fit on top of a standard spinner chuck, and the plate is held on top of the standard spinner chuck via vacuum. An O-ring around the recessed region may be necessary to achieve vacuum seal to the

standard spinner chuck such that the plate rotates with the standard spinner chuck.

4. Soft bake at 95°C for 4 minutes and 15 seconds.
5. Use backside alignment capability (infrared (IR) light probes beneath wafer, special IR transparent chuck, IR-sensitive camera) on the MJB4 to align through-hole pattern to features etched on the front side of the wafer.
6. Expose for 6 cycles, 12 seconds cycle time, 10 seconds wait time in between cycles. This is overexposure of the pattern even for this thickness of photoresist, but this ensures that the through-hole pattern fully develops.
7. Post-exposure bake for 2 minutes at 95°C.
8. Wait 10 minutes.
9. Develop using AZ 300 MIF developer. Development usually takes 10 minutes, but can vary significantly.
10. Inspect under microscope to ensure through-holes are fully developed. Re-align, re-expose, and re-develop if necessary.
11. Use crystal bond to mount on carrier wafer for etching. Crystal bond can be applied by placing carrier wafer on hot plate set to 100°C and then applying the crystal bond as one would apply glue using a glue stick. Avoid applying crystal bond in areas of the carrier wafer that would interact with features etched into the front side of the fabrication wafer to avoid scratching these features.
12. Cover any pin-holes in the photoresist or other non-uniformities in the photoresist coverage with Kapton tape.
13. Etch with recipe 3 (200 μm trench etch) on the Samco 800 for 400 cycles.

14. Dismount from carrier wafer and visually inspect (hold up to the light) to ensure all through-holes have gone through the wafer. Dismount is achieved by placing on a hot plate at 100°C and using a razor blade to pry the two wafers apart. If all the through-holes have not gone through, re-mount and etch another 50 to 100 cycles of recipe 3 on the Samco 800.
15. Re-mount onto carrier wafer and remove the Kapton tape carefully to avoid breaking the fabrication wafer.
16. Dismount from carrier wafer.
17. Use special spinner chuck from step 3. Spray HMDS and immediately spin off using spinner recipe 1.
18. Spin AZ5214 photoresist using recipe 1. Soft bake at 95°C for 5 minutes.
19. Load wafer on ring with dicing tape.
20. Dice using appropriate recipe on ADT Dicing Saw with blade designed for cutting silicon.
21. Carefully remove chip from dicing tape after exposing tape to ultraviolet light to decrease adhesiveness of the tape.
22. Spray chip with acetone and isopropanol. Blow dry under nitrogen.

Due to the long etch times and use of Kapton tape and crystal bond, the full Piranha clean is required before running experiments with chips fabricated using this method. The full Piranha clean process is detailed below.

Piranha Clean

1. Ensure no liquid solvent (acetone, isopropanol, ethanol) is present on chip. This process is performed with the chip loaded into a Fluoroware dipper basket.

2. Mix 96% sulfuric acid and 30% hydrogen peroxide in a 1:1 ratio in a glass beaker in sufficient quantity to completely immerse the chip.
3. Immerse the chip in solution for 15 minutes.
4. Rinse the chip under DI water and immerse the chip in large (>500 mL) Fluoroware beaker filled with DI water.
5. In a second large Fluoroware beaker, mix solution of 2% hydrofluoric (HF) acid by diluting 49% HF.
6. Remove the chip from the DI water beaker and immerse it in the 2% HF beaker for 1 minute.
7. Remove the chip from the 2% HF beaker and rinse under DI water. Immerse the chip in the Fluoroware beaker containing DI water.
8. Remove the dipper basket from the beaker and remove the chip from the dipper basket. Blow the chip dry under nitrogen.

Appendix C

Parts for Experimental Setup

This appendix details the parts necessary to set up and run the experiments described in Chapter 3 and Chapter 4.

C.1 Syringe Pump and Syringes

- Syringe pump: Fusion 200 High Precision Syringe Pump, Chemyx, Item Number 07200
- Syringes: 60 mL Disposable Syringe with Luer-Lok Tip; Fisher Scientific, Catalog No. 13-689-8

C.2 Parts for Manifold

O-Rings

- Inlet reservoirs: Metric Buna-N O-Ring 1 mm Width, 20 mm ID, McMaster Carr, Catalog No. 9262K618
- Outlet reservoirs: Metric Buna-N O-Ring 1 mm Width, 19 mm ID, McMaster Carr, Catalog No. 9262K617

Spring-Loaded Screws

- Spring: Type 302 Stainless Steel Compression Spring, 1.0" Length, .313" OD, .029" Wire Diameter, McMaster Carr, Catalog No. 1986K4
- Screw: 18-8 Stainless Steel Truss Head Slotted Machine Screw, 10-32 Thread, 2" Length, McMaster Carr, Catalog No. 19785A838
- Washer: Type 316 Stainless Steel Flat Washer, Number 10 Screw Size, 0.203" ID, 0.438" OD, McMaster Carr, Catalog No. 90107A011

Hydrophobic Filters

- Millex-FG Filter Unit, 0.2 μm , Hydrophobic PTFE, 25 mm, PVC, Ethylene Oxide Sterilized, Millipore, Catalog No. SLFG025LS

Fluidic Connections to Manifold

- Female Luer x 10-32 UNF Thread, Nylon, Cole Parmer, Catalog No. 45502-60

C.3 Tubing and Connectors

- Tubing: Peroxide-Cured Silicone Tubing, 1/8" o.d. x 1/16" i.d., Cole Parmer, Catalog No. EW-06411-62
- T-Valves: High-Pressure Stopcock, 1050 psi Max, 3-Way, Cole Parmer, Catalog No. EW-30526-34
- Female Barbed Luer: Female Luer x 1/16" Hose Barb Adapter, PP, Cole Parmer, Catalog No. EW-45508-00
- Male Barbed Luer: Male Luer x 1/16" Hose Barb, PP, Cole Parmer, Catalog No. EW-45518-22

Appendix D

Blood Protocols

This appendix details protocols used to obtain and handle blood used in the experiments in Chapter 3 and Chapter 4.

D.1 Blood Source

Blood is obtained in 8 mL ACD-coated tubes that are shipped overnight from Interstate Blood Bank (Memphis, TN). Blood is obtained from registered donors whose blood has cleared tests for common blood-borne viruses (HIV, Hepatitis B, etc.) within the previous six weeks, and only preliminary tests for these common blood-borne viruses are performed before the blood is shipped. Blood is shipped in an insulated container containing ice packs and is stored from the time of arrival to the time of experiment in a 4°C refrigerator.

D.2 Blood Preparation

Buffer for experiments involving blood is prepared as follows. We begin with phosphate buffered saline (PBS) from which the calcium and magnesium ions have been removed (Fisher Scientific, Catalog No. SH3002802). 1 g of bovine serum albumin

(BSA, Fraction V, Heat Shock Treated, Fisher Scientific, Catalog No. BP1600-100) is added for every 100 mL of PBS and is dissolved with gentle swirling. EDTA (Anhydrous, Crystalline, Sigma Aldrich, Catalog No. E6759-100G) is added to PBS such that the final concentration is at least 5 mM and not more than 7.5 mM. With a magnetic stir bar in the beaker, the EDTA typically takes at least 1 hour to dissolve. During this time, the buffer is also degassed using a vacuum pump. The solution is then filtered using a disposable filter unit with 0.2 μm pore size (Fisher Scientific, Catalog No. 09-741-04).

The water soluble form of PPACK dihydrochloride (Santa Cruz Biotechnology Inc., Catalog No. SC-201291A) is dissolved in water such that the final concentration is 0.2 mg/mL. The powder dissolves easily with gentle rocking of the centrifuge tube, and no magnetic stir bar is required. The solution is filtered through a Steriflip filter with 20 μm pore size (Millipore, Catalog No. SCNY00020) so that it does not need to be filtered before adding to the diluted blood before running the experiment.

Blood is diluted 1:3 in the buffer and filtered through a Steriflip filter with 20 μm pore size (Millipore, Catalog No. SCNY00020) to remove any clots that may have formed during transport. PPACK solution is then added such that the final concentration of PPACK is at least 40 μM and not more than 100 μM .

D.3 Counting Cells

Cells (and fluorescent polymer microspheres) are counted via haemocytometer (Figure D.1). The top of the haemocytometer is covered with a thin glass cover-slip to create a channel over a counting grid that is 100 μm deep. Approximately 10 μL of solution is injected into each of the loading ports such that the region over the counting grid is covered by fluid. A microscope is then used with either a 10X, 20X, or 60X objective lens to count cells over the counting grid region, which is enclosed

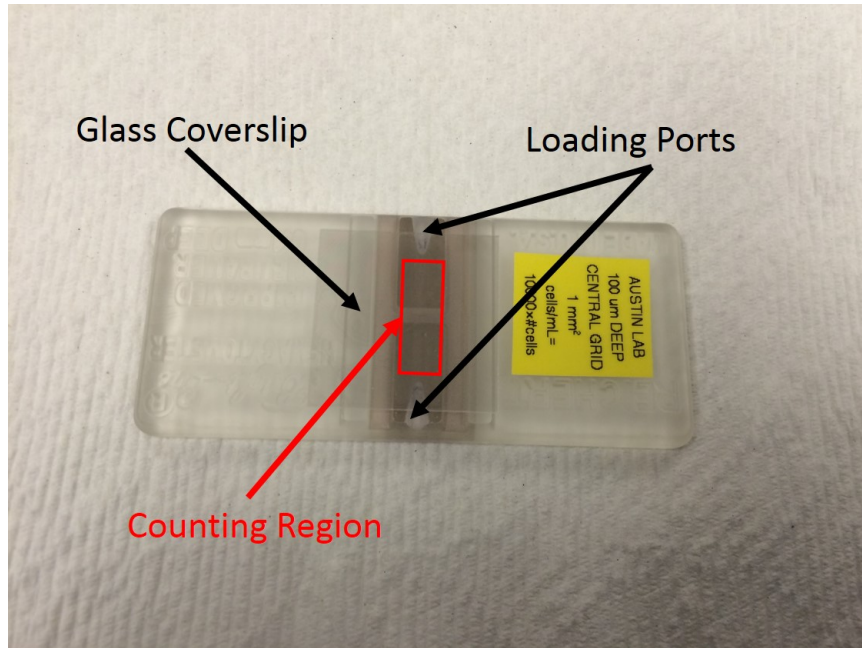


Figure D.1: The haemocytometer used to count cells in all of the experiments in Chapter 3 and Chapter 4 is shown above. The top of the haemocytometer is covered with a glass cover-slip as shown. Approximately $10 \mu\text{L}$ of solution is injected via micro-pipette into each of the loading ports. The haemocytometer is then placed on a microscope, and the cells are counted above a grid in the region inside the red rectangle. There are two counting grid regions inside the red rectangle, one for each loading port.

by the red rectangle in Figure D.1. In order to view fluorescently labelled cells, a microscope equipped with a mercury lamp is used.

Leukocytes that have been labelled with the fluorescent nucleic acid label, SYTO13, are shown above the central counting grid of the haemocytometer (enclosed by dotted red lines) in Figure D.2. A mercury lamp is used to excite fluorescence in the labelled leukocytes. The concentration of leukocytes in the solution being measured can be determined by counting the number of cells inside the dotted red square in Figure D.2, which has dimensions in the plane of 1 mm by 1 mm and a depth of $100 \mu\text{m}$. The concentration of leukocytes in the solution is this number multiplied by 10^4 per mL.

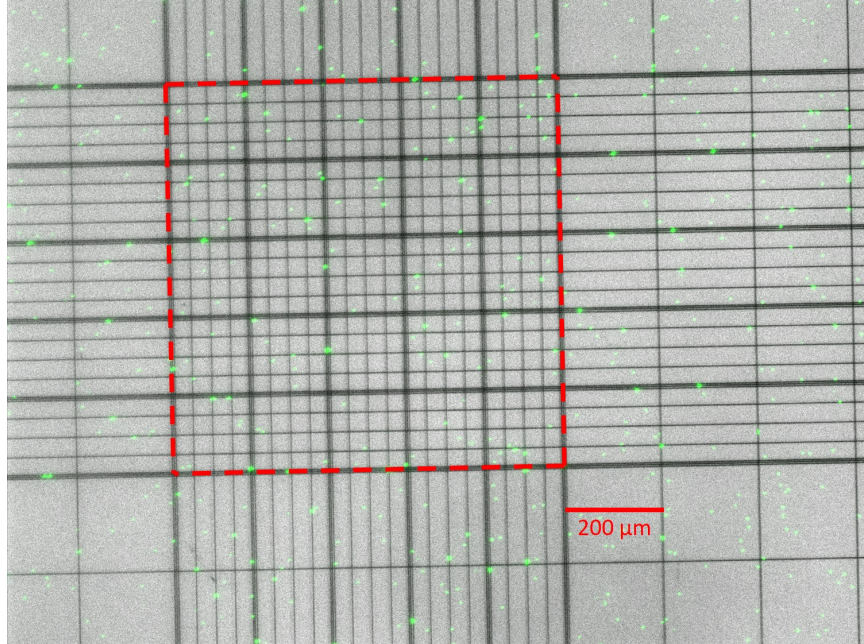


Figure D.2: Leukocytes labelled with SYTO13 (fluorescent nucleic acid label) are shown above the central counting grid (enclosed by the dotted red square), which is illuminated using a mercury lamp. The central counting grid is 1 mm by 1 mm in the plane, and the depth of the channel bounded above by the glass cover-slip is 100 μm . This means the concentration of leukocytes in the solution that is being measured here is the number of leukocytes in the square enclosed by the dotted red line multiplied by 10^4 per mL. Image courtesy of Yu Chen.

In measuring the concentration of leukocytes and erythrocytes in diluted whole blood, fluorescent labelling of leukocytes is used to distinguish between leukocytes and erythrocytes. Fluorescent labelling is also used to distinguish cancer cells from unlabelled leukocytes and erythrocytes. Significant dilution of the sample before it is loaded onto the haemocytometer is often required for measuring the concentration of erythrocytes. The concentration of erythrocytes can also be measured using counts within the smaller square grids within the large square enclosed by dotted red lines and multiplying by the appropriate number to get the total concentration. This is best performed with the 60X objective on the microscope. With the 60X objective, the erythrocytes can also be distinguished from the leukocytes by a very visible dot in the middle of the cell, resulting from the biconcave morphology of the erythrocytes.

Counting of leukocytes or cancer cells in blood can be made significantly easier with the removal of erythrocytes. In order to achieve this, we use erythrocyte lysis buffer (1X RBC Lysis Buffer, eBiosciences, Catalog No. 00-4333). 10 mL of lysis buffer is added to 1 mL of blood and incubated at room temperature for 10 minutes. The reaction is then stopped by adding 30 mL of 1X PBS. The solution is spun at 400g for 8 minutes, and the supernatant is removed via pipette. The pellet is then resuspended in PBS, and the cell count is performed via haemocytometer.

Appendix E

COMSOL Simulation Setup

In this appendix, we detail the COMSOL simulation setup used to perform the simulations in Chapter 4. All simulations are performed using the 2D laminar flow module. The following parameters should be set by clicking on the laminar flow tab in the model builder menu. The stationary form of the Navier-Stokes equation for incompressible fluids is used. The option to neglect the inertial term and the option to use the shallow channel approximation are both de-selected (not checked).

E.1 Schematic

The DLD array used in the simulations is shown in Figure E.1. The DLD array is 19 rows long (parallel to the flow direction) and 6 columns wide (perpendicular to the flow direction). Boundary conditions are no-slip at the walls and at the edges of the posts. Flow rate is set by uniform inflow velocity across the top of the array, and the bottom of the array is held uniformly at zero pressure. Array parameters are 60 μm asymmetric triangular posts, 40 μm gaps, and 1/20 tilt.

The uniform inflow velocity was related to the Reynolds number, Re , using a Bezier polygon across a gap in the middle of the array (the gap at the top of the red square shown in Figure E.1). By adding a 1D plot line graph and selecting this

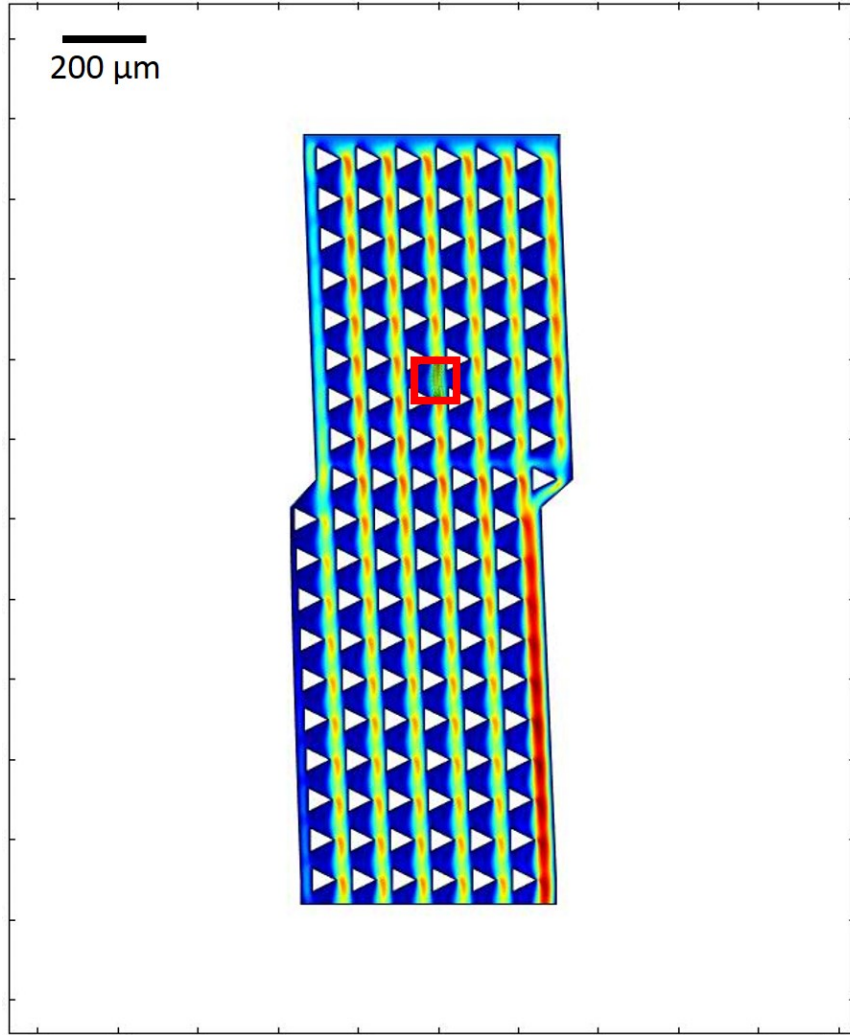


Figure E.1: The DLD array simulated using the 2D laminar flow module in COMSOL is 19 rows long (parallel to the flow direction) and 6 columns wide (perpendicular to the flow direction). Boundary conditions are no-slip at the walls and at the edges of the posts. Flow rate is set by uniform inflow velocity across the top of the array, and the bottom of the array is held uniformly at zero pressure. Array parameters are $60 \mu\text{m}$ asymmetric triangular posts, $40 \mu\text{m}$ gaps, and $1/20$ tilt. The red square shows the $100 \mu\text{m}$ by $100 \mu\text{m}$ unit cell that is analyzed in Section E.3.

Bezier polygon, the velocity across the gap could be simulated for different normal inflow velocities. The default expression and units for the y-axis of the 1D plot line graph should be velocity magnitude (spf.U) and m/s, respectively. The velocity used in the Reynolds number calculation is $2/3$ times the peak velocity in the gap. For Re of 20, the normal inflow velocity used is 0.224 m/s . The data from the 1D plot line

graph of the velocity in the gap can also be exported and opened in Matlab or Excel to determine the critical size using the method of D. Inglis et al. [35].

E.2 Shear Rate Simulations

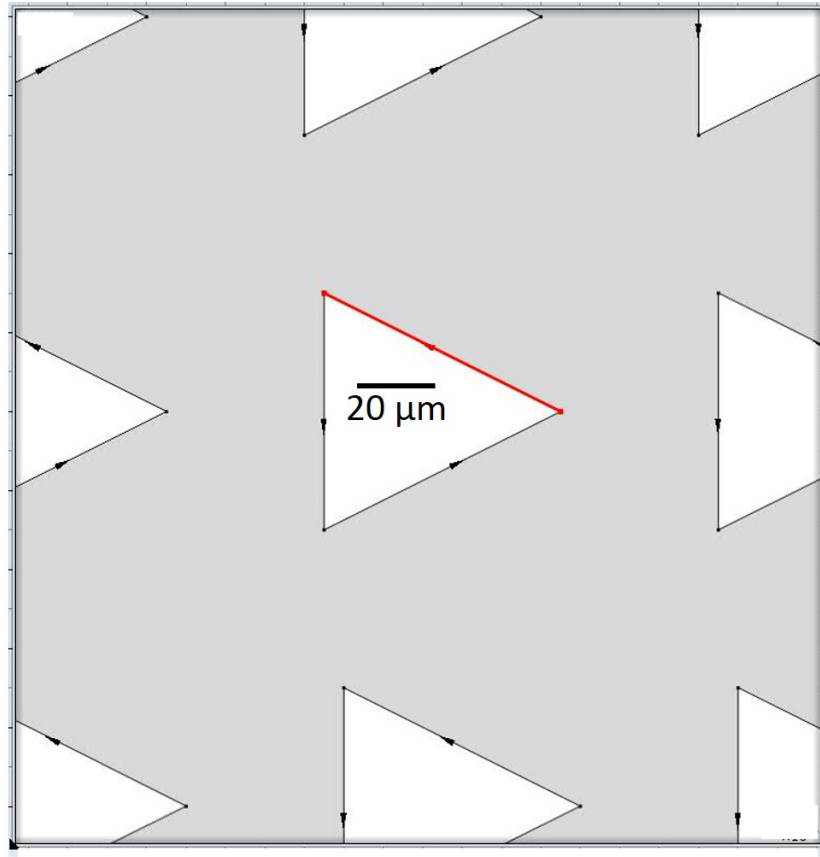


Figure E.2: The shear rate at the surface of the post against which a cell can be compressed can be obtained using the 1D plot line graph function and selecting the line shown in red for the asymmetric triangular post. The y-axis data and expression must be changed to `spf.sr` and `1/s`, respectively. The data from the 1D plot can then be exported as a text file that can be opened in Matlab or Excel for analysis.

The shear rate at the surface of the post against which the cell can be compressed can be calculated for a simulation that has already been run as follows. Add a 1D plot group to the results, and select line graph. The expression and units for the y-data should be set to `spf.sr` and `1/s`, respectively. The edge or multiple edges of

the post can be selected simply by clicking on the edge, as shown in Figure E.2, and added to the selection section of the line graph options. Data from the 1D plot can be exported as a text file for analysis in Matlab or Excel by right-clicking on the line graph tab and adding plot data to export.

E.3 Centripetal Acceleration Simulations

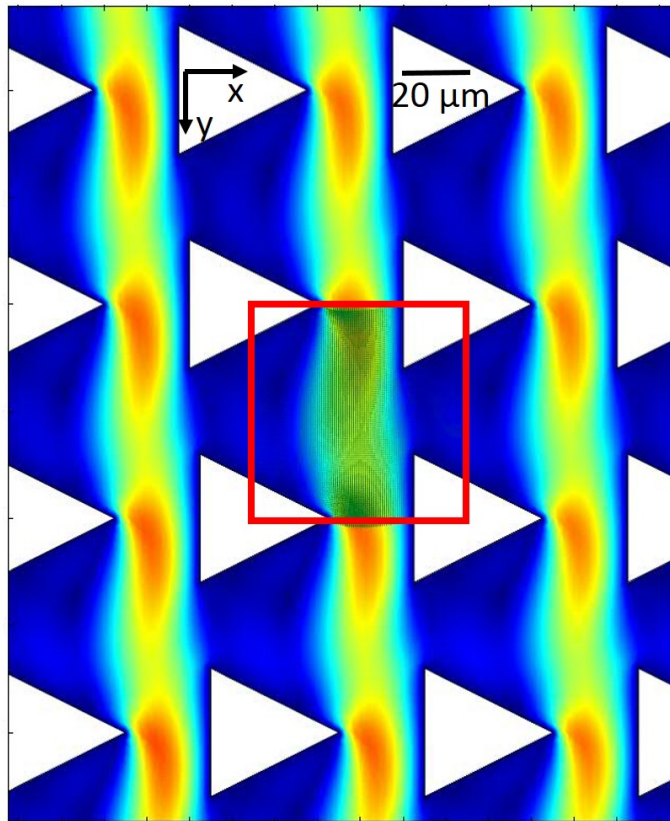


Figure E.3: Magnified image of the region within and around the red square in Figure E.1 that is used in the fluid centripetal acceleration simulations in Chapter 4. The green arrows are from the arrow surface that allows extraction of the x and y components of the velocity at $1 \mu\text{m}$ intervals within the red square, which has dimensions of $100 \mu\text{m}$ by $100 \mu\text{m}$. Data from the arrow surface is exported as a text file, and the centripetal acceleration of the fluid as it travels from one gap to the next in the direction of the flow is computed numerically in Matlab.

We seek to evaluate the fluid centripetal acceleration (acceleration perpendicular to the streamlines) as fluid travels from one gap to the next in the direction of the flow. To do this, we need to know the x and y components of the velocity at evenly-spaced points in a grid covering a unit cell of the DLD array ($100\ \mu\text{m}$ by $100\ \mu\text{m}$ in this case). One way to obtain this data is to add an arrow surface on top of the 2D velocity surface plot in COMSOL. This can be done by right-clicking on the velocity tab under the results section in the model builder menu, and clicking on arrow surface. The range of coordinates and the spacing within the range at which arrows will be placed can be specified in the menu for the arrow surface. We specify a $100\ \mu\text{m}$ by $100\ \mu\text{m}$ area with $1\ \mu\text{m}$ spacing along each axis that stretches vertically from one gap to the next in the direction of the flow and is centered horizontally about the center of the first gap. This arrow surface is bounded by the red square in Figure E.3, and the larger arrows, indicating higher fluid velocity, are visible in green in the gap. The velocity data from this arrow surface is then exported as a text file for analysis in Matlab by right-clicking on the arrow surface tab and adding the plot data to export.

Bibliography

- [1] Mohamed Al-Fandi, Mohammad Al-Rousan, Mohammad AK Jaradat, and Lina Al-Ebbini. New design for the separation of microorganisms using microfluidic deterministic lateral displacement. *Robotics and computer-integrated manufacturing*, 27(2):237–244, 2011.
- [2] Jennie Bäck, Markus Huber Lang, Graciela Elgue, Miriam Kalbitz, Javier Sanchez, Kristina Nilsson Ekdahl, and Bo Nilsson. Distinctive regulation of contact activation by antithrombin and c1-inhibitor on activated platelets and material surfaces. *Biomaterials*, 30(34):6573–6580, 2009.
- [3] Manuel Balvin, Eunkyung Sohn, Tara Iracki, German Drazer, and Joelle Frechette. Directional locking and the role of irreversible interactions in deterministic hydrodynamics separations in microfluidic devices. *Physical review letters*, 103(7):078301, 2009.
- [4] Jason P Beech, Stefan H Holm, Karl Adolfsson, and Jonas O Tegenfeldt. Sorting cells by size, shape and deformability. *Lab on a Chip*, 12(6):1048–1051, 2012.
- [5] Jason P Beech, Peter Jönsson, and Jonas O Tegenfeldt. Tipping the balance of deterministic lateral displacement devices using dielectrophoresis. *Lab on a Chip*, 9(18):2698–2706, 2009.
- [6] Timothy J Bowman, German Drazer, and Joelle Frechette. Inertia and scaling in deterministic lateral displacement. *Biomicrofluidics*, 7(6):064111, 2013.
- [7] Isabelle Cantat and Chaouqi Misbah. Lift force and dynamical unbinding of adhering vesicles under shear flow. *Physical review letters*, 83(4):880, 1999.
- [8] Sunghwan Chang and Young-Ho Cho. A continuous multi-size particle separator using negative dielectrophoretic virtual pillars induced by a planar spot electrode array. In *Micro Electro Mechanical Systems, 2007. MEMS. IEEE 20th International Conference on*, pages 19–22. IEEE, 2007.
- [9] Yu Chen, Joseph D’Silva, Robert H Austin, and James C Sturm. Microfluidic chemical processing with on-chip washing by deterministic lateral displacement arrays with separator walls. *Biomicrofluidics*, 9(5):054105, 2015.
- [10] Jongchan Choi, Ji-chul Hyun, and Sung Yang. On-chip extraction of intracellular molecules in white blood cells from whole blood. *Scientific reports*, 5, 2015.

- [11] Thomas V Colace, Garth W Tormoen, Owen JT McCarty, and Scott L Diamond. Microfluidics and coagulation biology. *Annual review of biomedical engineering*, 15:283, 2013.
- [12] David J Collins, Tuncay Alan, and Adrian Neild. Particle separation using virtual deterministic lateral displacement (vdld). *Lab on a Chip*, 14(9):1595–1603, 2014.
- [13] Massimo Cristofanilli, G Thomas Budd, Matthew J Ellis, Alison Stopeck, Jeri Matera, M Craig Miller, James M Reuben, Gerald V Doyle, W Jeffrey Allard, Leon WMM Terstappen, et al. Circulating tumor cells, disease progression, and survival in metastatic breast cancer. *New England Journal of Medicine*, 351(8):781–791, 2004.
- [14] John A Davis, David W Inglis, Keith J Morton, David A Lawrence, Lotien R Huang, Stephen Y Chou, James C Sturm, and Robert H Austin. Deterministic hydrodynamics: taking blood apart. *Proceedings of the National Academy of Sciences*, 103(40):14779–14784, 2006.
- [15] John Alan Davis. *Microfluidic separation of blood components through deterministic lateral displacement*. PhD thesis, Princeton University, 2008.
- [16] Raghavendra Devendra and German Drazer. Deterministic fractionation of binary suspensions moving past a line of microposts. *Microfluidics and Nanofluidics*, 17(3):519–526, 2014.
- [17] Dino Di Carlo. Inertial microfluidics. *Lab on a Chip*, 9(21):3038–3046, 2009.
- [18] Joseph D’Silva, Robert H Austin, and James C Sturm. Inhibition of clot formation in deterministic lateral displacement arrays for processing large volumes of blood for rare cell capture. *Lab on a Chip*, 15(10):2240–2247, 2015.
- [19] Alexander Farutin and Chaouqi Misbah. Analytical and numerical study of three main migration laws for vesicles under flow. *Physical review letters*, 110(10):108104, 2013.
- [20] RA Freitas Jr. Nanomedicine, volume i: Basic capabilities. landes bioscience, georgetown, tx, 1999.
- [21] Thomas M Geislinger and Thomas Franke. Sorting of circulating tumor cells (mv3-melanoma) and red blood cells using non-inertial lift. *Biomicrofluidics*, 7(4):044120, 2013.
- [22] Thomas M Geislinger and Thomas Franke. Hydrodynamic lift of vesicles and red blood cells in flow—from fähræus & lindqvist to microfluidic cell sorting. *Advances in colloid and interface science*, 208:161–176, 2014.
- [23] FO Griffin and A Meisen. Impaction of spherical particles on cylinders at moderate reynolds numbers. *Chemical Engineering Science*, 28(12):2155–2164, 1973.

- [24] Johan WM Heemskerk, Edouard M Bevers, Theo Lindhout, et al. Platelet activation and blood coagulation. *THROMBOSIS AND HAEMOSTASIS-STUTTGART*-, 88(2):186–194, 2002.
- [25] JD Hellums, DM Peterson, NA Stathopoulos, JL Moake, and TD Giorgio. Studies on the mechanisms of shear-induced platelet activation. In *Cerebral ischemia and hemorheology*, pages 80–89. Springer, 1987.
- [26] Stefan H Holm, Jason P Beech, Michael P Barrett, and Jonas O Tegenfeldt. Separation of parasites from human blood using deterministic lateral displacement. *Lab on a Chip*, 11(7):1326–1332, 2011.
- [27] Pål A Holme, Una Ørvim, Maria JAG Hamers, Nils O Solum, Frank R Brosstad, R Marius Barstad, and Kjell S Sakariassen. Shear-induced platelet activation and platelet microparticle formation at blood flow conditions as in arteries with a severe stenosis. *Arteriosclerosis, thrombosis, and vascular biology*, 17(4):646–653, 1997.
- [28] David Holmes, Graeme Whyte, Joe Bailey, Nuria Vergara-Irigaray, Andrew Ekpenyong, Jochen Guck, and Tom Duke. Separation of blood cells with differing deformability using deterministic lateral displacement. *Interface focus*, 4(6):20140011, 2014.
- [29] Han Wei Hou, Ali Asgar S Bhagat, Alvin Guo Lin Chong, Pan Mao, Kevin Shyong Wei Tan, Jongyoon Han, and Chwee Teck Lim. Deformability based cell margination-a simple microfluidic design for malaria-infected erythrocyte separation. *Lab on a Chip*, 10(19):2605–2613, 2010.
- [30] Lotien Richard Huang, Edward C Cox, Robert H Austin, and James C Sturm. Continuous particle separation through deterministic lateral displacement. *Science*, 304(5673):987–990, 2004.
- [31] Pin Y Huang and J David Hellums. Aggregation and disaggregation kinetics of human blood platelets: Part iii. the disaggregation under shear stress of platelet aggregates. *Biophysical journal*, 65(1):354, 1993.
- [32] R Huang, TA Barber, MA Schmidt, RG Tompkins, M Toner, DW Bianchi, R Kapur, and WL Flejter. A microfluidics approach for the isolation of nucleated red blood cells (nrbc) from the peripheral blood of pregnant women. *Prenatal diagnosis*, 28(10):892–899, 2008.
- [33] Soojung Claire Hur, Nicole K Henderson-MacLennan, Edward RB McCabe, and Dino Di Carlo. Deformability-based cell classification and enrichment using inertial microfluidics. *Lab on a Chip*, 11(5):912–920, 2011.
- [34] David W Inglis. Efficient microfluidic particle separation arrays. *Applied Physics Letters*, 94(1):013510, 2009.

- [35] David W Inglis, John A Davis, Robert H Austin, and James C Sturm. Critical particle size for fractionation by deterministic lateral displacement. *Lab on a Chip*, 6(5):655–658, 2006.
- [36] David W Inglis, John A Davis, Thomas J Zieziulewicz, David A Lawrence, Robert H Austin, and James C Sturm. Determining blood cell size using microfluidic hydrodynamics. *Journal of immunological methods*, 329(1):151–156, 2008.
- [37] David W Inglis, Megan Lord, and Robert E Nordon. Scaling deterministic lateral displacement arrays for high throughput and dilution-free enrichment of leukocytes. *Journal of Micromechanics and Microengineering*, 21(5):054024, 2011.
- [38] David W Inglis, Robert Riehn, RH Austin, and JC Sturm. Continuous microfluidic immunomagnetic cell separation. *Applied Physics Letters*, 85(21):5093–5095, 2004.
- [39] Mingliang Jiang, Kostyantyn Budzan, and German Drazer. Fractionation by shape in deterministic lateral displacement microfluidic devices. *Microfluidics and Nanofluidics*, 19(2):427–434, 2015.
- [40] Nezihi Murat Karabacak, Philipp S Spuhler, Fabio Fachin, Eugene J Lim, Vincent Pai, Emre Ozkumur, Joseph M Martel, Nikola Kojic, Kyle Smith, Pin-i Chen, et al. Microfluidic, marker-free isolation of circulating tumor cells from blood samples. *Nature protocols*, 9(3):694–710, 2014.
- [41] F Khodaei, S Movahed, N Fatouraei, and F Daneshmand. Numerical simulation of separation of circulating tumor cells from blood stream in deterministic lateral displacement (dld) microfluidic channel. *Journal of Mechanics*, pages 1–9, 2015.
- [42] Timm Krüger, David Holmes, and Peter V Coveney. Deformability-based red blood cell separation in deterministic lateral displacement devices—a simulation study. *Biomicrofluidics*, 8(5):054114, 2014.
- [43] T Kulrattanarak, RGM Van der Sman, YS Lubbersen, CGPH Schroën, HTM Pham, PM Sarro, and RM Boom. Mixed motion in deterministic ratchets due to anisotropic permeability. *Journal of colloid and interface science*, 354(1):7–14, 2011.
- [44] T Kulrattanarak, RGM van der Sman, CGPH Schroën, and RM Boom. Analysis of mixed motion in deterministic ratchets via experiment and particle simulation. *Microfluidics and Nanofluidics*, 10(4):843–853, 2011.
- [45] Thomas MH Lee, Debbie HY Lee, Connie YN Liaw, Alex IK Lao, and I-Ming Hsing. Detailed characterization of anodic bonding process between glass and thin-film coated silicon substrates. *Sensors and Actuators A: Physical*, 86(1):103–107, 2000.

- [46] Xiujun James Li and Yu Zhou. *Microfluidic devices for biomedical applications*. Elsevier, 2013.
- [47] Zongbin Liu, Fei Huang, Jinghui Du, Weiliang Shu, Hongtao Feng, Xiaoping Xu, and Yan Chen. Rapid isolation of cancer cells using microfluidic deterministic lateral displacement structure. *Biomicrofluidics*, 7(1):011801, 2013.
- [48] Brian R Long, Martin Heller, Jason P Beech, Heiner Linke, Henrik Bruus, and Jonas O Tegenfeldt. Multidirectional sorting modes in deterministic lateral displacement devices. *Physical Review E*, 78(4):046304, 2008.
- [49] Kevin Loutherbach, Kevin S Chou, Jonathan Newman, Jason Puchalla, Robert H Austin, and James C Sturm. Improved performance of deterministic lateral displacement arrays with triangular posts. *Microfluidics and nanofluidics*, 9(6):1143–1149, 2010.
- [50] Kevin Loutherbach, Joseph D’Silva, Liyu Liu, Amy Wu, Robert H Austin, and James C Sturm. Deterministic separation of cancer cells from blood at 10 ml/min. *AIP advances*, 2(4):042107, 2012.
- [51] Kevin Loutherbach, Jason Puchalla, Robert H Austin, and James C Sturm. Deterministic microfluidic ratchet. *Physical review letters*, 102(4):045301, 2009.
- [52] Bo Lu, Tong Xu, Siyang Zheng, Amir Goldkorn, and Yu-Chong Tai. Parylene membrane slot filter for the capture, analysis and culture of viable circulating tumor cells. 2010.
- [53] Hang Lu, Lily Y Koo, Wechung M Wang, Douglas A Lauffenburger, Linda G Griffith, and Klavs F Jensen. Microfluidic shear devices for quantitative analysis of cell adhesion. *Analytical chemistry*, 76(18):5257–5264, 2004.
- [54] YS Lubbersen, JP Dijkshoorn, MAI Schutyser, and RM Boom. Visualization of inertial flow in deterministic ratchets. *Separation and Purification Technology*, 109:33–39, 2013.
- [55] YS Lubbersen, F Fasaei, P Kroon, RM Boom, and MAI Schutyser. Particle suspension concentration with sparse obstacle arrays in a flow channel. *Chemical Engineering and Processing: Process Intensification*, 95:90–97, 2015.
- [56] YS Lubbersen, MAI Schutyser, and RM Boom. Suspension separation with deterministic ratchets at moderate reynolds numbers. *Chemical engineering science*, 73:314–320, 2012.
- [57] Jane A May and Stanley Heptinstall. Effects of anticoagulants used during blood collection on human platelet function. *Platelets and Megakaryocytes: Volume 1: Functional Assays*, pages 3–11, 2004.

- [58] Songdong Meng, Debasish Tripathy, Eugene P Frenkel, Sanjay Shete, Elizabeth Z Naftalis, James F Huth, Peter D Beitsch, Marilyn Leitch, Susan Hoover, David Euhus, et al. Circulating tumor cells in patients with breast cancer dormancy. *Clinical cancer research*, 10(24):8152–8162, 2004.
- [59] Warwick S Nesbitt, Erik Westein, Francisco Javier Tovar-Lopez, Elham Tolouei, Arnan Mitchell, Jia Fu, Josie Carberry, Andreas Fouras, and Shaun P Jackson. A shear gradient-dependent platelet aggregation mechanism drives thrombus formation. *Nature medicine*, 15(6):665–673, 2009.
- [60] Sven Nylander and Christer Mattsson. Thrombin-induced platelet activation and its inhibition by anticoagulants with different modes of action. *Blood coagulation & fibrinolysis*, 14(2):159–167, 2003.
- [61] Nicole Pamme. Continuous flow separations in microfluidic devices. *Lab on a Chip*, 7(12):1644–1659, 2007.
- [62] Ryan S Pawell, David W Inglis, Tracie J Barber, and Robert A Taylor. Manufacturing and wetting low-cost microfluidic cell separation devices. *Biomicrofluidics*, 7(5):056501, 2013.
- [63] D Mo Peterson, NA Stathopoulos, TD Giorgio, JD Hellums, and JL Moake. Shear-induced platelet aggregation requires von willebrand factor and platelet membrane glycoproteins ib and iib-iiia. *Blood*, 69(2):625–628, 1987.
- [64] Filip Petersson, Andreas Nilsson, Henrik Jönsson, and Thomas Laurell. Carrier medium exchange through ultrasonic particle switching in microfluidic channels. *Analytical chemistry*, 77(5):1216–1221, 2005.
- [65] Hoa TM Pham, T Kulrattanak, RGM van der Sman, CGPH Schroën, RM Boom, and PM Sarro. Deterministic ratchets for particle separation fabricated with si mems technology. *Procedia Chemistry*, 1(1):345–348, 2009.
- [66] Marie Pødenphant, Neil Ashley, Kamila Koprowska, Kalim U Mir, Maksim Zalkovskij, Brian Bilenberg, Walter Bodmer, Anders Kristensen, and Rodolphe Marie. Separation of cancer cells from white blood cells by pinched flow fractionation. *Lab on a Chip*, 15(24):4598–4606, 2015.
- [67] Edward M Purcell. Life at low reynolds number. *Am. J. Phys*, 45(1):3–11, 1977.
- [68] Raymond Quek, Duc Vinh Le, and K-H Chiam. Separation of deformable particles in deterministic lateral displacement devices. *Physical Review E*, 83(5):056301, 2011.
- [69] JM Ramstack, L Zuckerman, and LF Mockros. Shear-induced activation of platelets. *Journal of biomechanics*, 12(2):113–125, 1979.

- [70] Shashi Ranjan, Kerwin Kwek Zeming, Roland Jureen, Dale Fisher, and Yong Zhang. Old pillar shape design for efficient separation of spherical and non-spherical bioparticles. *Lab on a Chip*, 14(21):4250–4262, 2014.
- [71] Sabine Riethdorf, Herbert Fritsche, Volkmar Müller, Thomas Rau, Christian Schindlbeck, Brigitte Rack, Wolfgang Janni, Cornelia Coith, Katrin Beck, Fritz Jänicke, et al. Detection of circulating tumor cells in peripheral blood of patients with metastatic breast cancer: a validation study of the cellsearch system. *Clinical Cancer Research*, 13(3):920–928, 2007.
- [72] P Sajeesh and Ashis Kumar Sen. Particle separation and sorting in microfluidic devices: a review. *Microfluidics and nanofluidics*, 17(1):1–52, 2014.
- [73] David J Schneider, Patricia Q Baumann, Deborah A Whitaker, and Burton E Sobel. Variation in the ability of glycoprotein iib-iiia antagonists to exert and maintain their inhibitory effects on the binding of fibrinogen. *Journal of cardiovascular pharmacology*, 46(1):41–45, 2005.
- [74] Elodie Sollier, Derek E Go, James Che, Daniel R Gossett, Sean O’Byrne, Westbrook M Weaver, Nicolas Kummer, Matthew Rettig, Jonathan Goldman, Nicholas Nickols, et al. Size-selective collection of circulating tumor cells using vortex technology. *Lab on a Chip*, 14(1):63–77, 2014.
- [75] Pilar Solves, Vicente Mirabet, Amando Blanquer, Francisco Delgado-Rosas, Dolores Planelles, Margarita Andrade, Francisco Carbonell-Uberos, M Angeles Soler, and Roberto Roig. A new automatic device for routine cord blood banking: critical analysis of different volume reduction methodologies. *Cytotherapy*, 11(8):1101–1107, 2009.
- [76] Hetty T Spijker, Rolf Bos, Henk J Busscher, Theo G van Kooten, and Wim van Oeveren. Platelet adhesion and activation on a shielded plasma gradient prepared on polyethylene. *Biomaterials*, 23(3):757–766, 2002.
- [77] Claudiu A Stan, Audrey K Ellerbee, Laura Guglielmini, Howard A Stone, and George M Whitesides. The magnitude of lift forces acting on drops and bubbles in liquids flowing inside microchannels. *Lab on a Chip*, 13(3):365–376, 2013.
- [78] Daniel V Surbek, Eva Visca, Christian Steinmann, André Tichelli, Stefan Schatta, Sinuhe Hahn, Alois Gratwohl, and Wolfgang Holzgreve. Umbilical cord blood collection before placental delivery during cesarean delivery increases cord blood volume and nucleated cell number available for transplantation. *American journal of obstetrics and gynecology*, 183(1):218–221, 2000.
- [79] Subra Suresh, J Spatz, JP Mills, Alexandre Micoulet, M Dao, CT Lim, M Beil, and T Seufferlein. Connections between single-cell biomechanics and human disease states: gastrointestinal cancer and malaria. *Acta biomaterialia*, 1(1):15–30, 2005.

- [80] Junya Takagi, Masumi Yamada, Masahiro Yasuda, and Minoru Seki. Continuous particle separation in a microchannel having asymmetrically arranged multiple branches. *Lab on a Chip*, 5(7):778–784, 2005.
- [81] Pankaj Vadgama. *Surfaces and interfaces for biomaterials*. CRC Press, 2005.
- [82] Virginia VanDelinder and Alex Groisman. Perfusion in microfluidic cross-flow: separation of white blood cells from whole blood and exchange of medium in a continuous flow. *Analytical Chemistry*, 79(5):2023–2030, 2007.
- [83] Majid Ebrahimi Warkiani, Guofeng Guan, Khoo Bee Luan, Wong Cheng Lee, Ali Asgar S Bhagat, Parthiv Kant Chaudhuri, Daniel Shao-Weng Tan, Wan Teck Lim, Soo Chin Lee, Peter CY Chen, et al. Slanted spiral microfluidics for the ultra-fast, label-free isolation of circulating tumor cells. *Lab on a Chip*, 14(1):128–137, 2014.
- [84] Jeffrey I Weitz. Activation of blood coagulation by plaque rupture: mechanisms and prevention. *The American journal of cardiology*, 75(6):18B–22B, 1995.
- [85] JI Weitz, M Hudoba, D Massel, J Maraganore, and J Hirsh. Clot-bound thrombin is protected from inhibition by heparin-antithrombin iii but is susceptible to inactivation by antithrombin iii-independent inhibitors. *Journal of Clinical Investigation*, 86(2):385, 1990.
- [86] Masumi Yamada, Megumi Nakashima, and Minoru Seki. Pinched flow fractionation: continuous size separation of particles utilizing a laminar flow profile in a pinched microchannel. *Analytical chemistry*, 76(18):5465–5471, 2004.
- [87] Shangjun Ye, Xueming Shao, Zhaosheng Yu, and Wenguang Yu. Effects of the particle deformability on the critical separation diameter in the deterministic lateral displacement device. *Journal of Fluid Mechanics*, 743:60–74, 2014.
- [88] Kerwin Kwek Zeming, Shashi Ranjan, and Yong Zhang. Rotational separation of non-spherical bioparticles using i-shaped pillar arrays in a microfluidic device. *Nature communications*, 4:1625, 2013.
- [89] Kerwin Kwek Zeming, Thoriq Salafi, Chia-Hung Chen, and Yong Zhang. Asymmetrical deterministic lateral displacement gaps for dual functions of enhanced separation and throughput of red blood cells. *Scientific reports*, 6, 2016.
- [90] Wen Zeng, Ian Jacobi, David J Beck, Songjing Li, and Howard A Stone. Characterization of syringe-pump-driven induced pressure fluctuations in elastic microchannels. *Lab on a Chip*, 15(4):1110–1115, 2015.
- [91] Boyang Zhang, James V Green, Shashi K Murthy, and Milica Radisic. Label-free enrichment of functional cardiomyocytes using microfluidic deterministic lateral flow displacement. *PLoS One*, 7(5):e37619, 2012.

- [92] Zunmin Zhang, Ewan Henry, Gerhard Gompper, and Dmitry A Fedosov. Behavior of rigid and deformable particles in deterministic lateral displacement devices with different post shapes. *The Journal of chemical physics*, 143(24):243145, 2015.
- [93] Siyang Zheng, Raylene Yung, Yu-Chong Tai, and Harvey Kasdan. Deterministic lateral displacement mems device for continuous blood cell separation. In *Micro Electro Mechanical Systems, 2005. MEMS 2005. 18th IEEE International Conference on*, pages 851–854. IEEE, 2005.